Supplementary Materials for

Improved compactness of self-assembled monolayers through Coulomb interaction enables highly efficient and stable perovskite solar cells

Qi Cao[1,2]†, Tao Du[1,3]†, Zuolin Zhang[4]†, Jianjun Mei[1], Xilai He[2], Zhenhuang Su[5], Guangpeng Feng[2], Bochun Kang[1], Junkang Hou[2], Xingyan Wang[2], Cong Chen[4,*], Jun Yin[1,*], Xuanhua Li[2,*], and Feng Yan[1,6*]

[1] Department of Applied Physics, Research Centre for Organic Electronics, The Hong Kong Polytechnic University, Hung Hom, Kowloon, Hong Kong SAR 999077, P. R. China.

[2] State Key Laboratory of Solidification Processing, Center for Nano Energy Materials, School of Materials Science and Engineering, Northwestern Polytechnical University, Xi´an, 710072, China.

[3] Key Lab of Smart Prevention and Mitigation of Civil Engineering Disasters of the Ministry of Industry and Information Technology, Harbin Institute of Technology, Harbin 150090, P. R. China.

[4] State Key Laboratory of Reliability and Intelligence of Electrical Equipment, School of Materials Science and Engineering, Hebei University of Technology, Tianjin 300401, P. R. China.

[5] Shanghai Synchrotron Radiation Facility (SSRF), Shanghai Advanced Research Institute, Chinese Academy of Sciences 239 Zhangheng Road, Shanghai 201204, P. R. China.

[6] Research Institute of Intelligent Wearable Systems, The Hong Kong Polytechnic University, Hung Hom, Kowloon, Hong Kong SAR 999077, P. R. China.

† These authors contribute equally to this work.

* E-mail: apafyan@polyu.edu.hk, lixh32@nwpu.edu.cn, jun.yin@polyu.edu.hk, chencong@hebut.edu.cn

Table of contents:

Materials and Methods

Materials: Nickel nitrate hexahydrate ($Ni(NO_3)_2 \cdot 6H_2O$, 99.999%), chlorobenzene (CB, 99.8%), anhydrous dimethyl sulfoxide (DMSO, 99.8%), and N,N-dimethylformamide (DMF, 99.8%) were purchased from Sigma-Aldrich. Lead iodide (PbI_2), cesium iodide (CsI), methylammonium iodide (MAI), lead bromide ($PbBr_2$), bathocuproine (BCP), and methylamine hydrochloride (MACl) were purchased from Xi'an Yuri Solar Co. Ltd. Phenethylammonium bromide (PEABr), formamidine iodide (FAI) were purchased from Greatcell Solar Materials. Lithium hydroxide (LiOH, 99.99%), sodium hydroxide (NaOH, 99.9%), and potassium hydroxide (KOH, 99.99%) were purchased from Aladdin. [4-(3,6-dimethyl-9H-carbazol-9yl)butyl]phosphonic acid (Me-4PACz), [2-(9H-carbazol-9yl)ethyl] phosphonic acid (2PACz), and [4-(3,6-dimethoxy-9H-carbazol-9-yl)butyl]phosphonic acid (MeO-4PACz) were obtained from TCI America.

Materials Synthesis: Nickel oxide nanoparticles (NiO_x-NPs) were synthesized according to a previous literature [1]. 1.7 M $Cs_{0.05}MA_{0.05}FA_{0.9}PbI_3$ perovskite precursors were prepared by dissolving 0.085 mmol CsI, 0.085 mmol MAI, 1.53 mmol FAI, and 1.7 mmol PbI_2 in DMF: DMSO (4:1 volume ratio, v: v), 5% $MAPbCl_3$ excess were added to improve the quality of perovskite films. The precursor solutions were stirred at 60 °C for 1 h and then filtered using a 0.22 μm polytetrafluoroethylene membrane before use.

Inverted (p-i-n) Solar Cell Fabrication: ITO glasses were continuously washed in an ultrasonic bath for 15 min in detergent-deionized water solution, acetone and ethanol, respectively. The ITO glasses were dried with N_2 and then treated with UV-ozone for 7 min to increase hydrophilicity. NiO_x-NPs (20 mg ml^{-1} in H_2O) was deposited on ITO at 2000 rpm for 30 s and then heated at 100 °C for 10 min. The coated ITO was then moved to a glove box. The LiOH-reacted Me-4PACz were fabricated by spin-coating the Me-4PACz (0.3 mg mL^{-1} in C_2H_5OH) and LiOH (molar ratio=1:0, 1:0.25, 1:0.5, 1:1, 1:2) on NiO_x-NPs substrates at 4000 rpm for 30 s, followed by thermal annealing at 100 ℃ for 10 min. After that, the substrates needed to be washed

with ethanol through spin-coating at 4000 rpm for 30 s, then annealing at 100 °C for 5 min. The perovskite solution was spin coated on the Me-4PACz or LiOH-reacted Me-4PACz according to procedure that was increased from 1000 rpm for 10 s to 5000 rpm for 30 s, dropping 150 μL chlorobenzene antisolvent for 10 s before the end of the procedure. Then heated at 110 °C for 10 min to obtain the bright perovskite film. PEABr with concentration of 1 mg/ml in IPA and DMSO solution (volume ratio 200:1) was dynamically spin-coated on top (4000 rpm, 30 s) and annealed at 100 °C for 5 min. After that, the PCBM and C_{60} mixed solution (25 mg mL^{-1}, 4/1, w/w, 1mL CB) was spin-coated on the PEABr at speed of 3000 rpm for 30 s. Next, BCP (0.5 mg mL^{-1} in IPA) was spin coated on it at 5000 rpm for 30 s. Finally, fabrication of the devices was accomplished by thermally evaporating Ag (100 nm) electrodes (0.0535 cm^2 mask area). A 100-nm thick magnesium fluoride layer was deposited on the back of ITO substrate for transmittance enhancement.

Solar Cell Characterization: The SEM images of perovskite films and cross-sectional devices were obtained using Tescan MAIA3. GIXRD patterns of the perovskite films were gained by using Rigaku SmartLab 9kW. The crystallization of the perovskite film was characterized via grazing-incidence wide-angle X-ray scattering (GIWAXS, BL14B1 beamline of the Shanghai Synchrotron Radiation Facility (SSRF) using X-ray with a wavelength of 0.6887 Å). XPS and UPS measurements were obtained on a Thermo Fisher Scientific Nexsa. The *J-V* curves of PSCs were recorded under AM 1.5 G (100 mW cm^{-2}) solar illumination from a Elitetech solar simulator, and the scan rate corresponding to the curve was 0.02 V s^{-1}. EQE spectra of the PSCs were obtained from ZOLIX Optoelectronic Device Quantum Efficiency Measurement. FT-IR spectra were measured on a Jasco FT-IR-6100 in a wavelength range of 4000 to 650 cm^{-1}. Admittance spectroscopy (AS) was conducted using an impedance analyzer (ZAHNER Stat.). Mott-Schottky analysis was carried out on an electrochemical workstation (Chenhua 760) and was measured in the 0-1.5 V voltage range and 1000 Hz frequency under dark. KPFM and AFM were conducted

with an Asylum Research AFM (OXFORD). TOF-SIMS of films were analyzed using a TOF-SIMS5-100 with the sputter ion of 5 k eV Cs^+ cluster. The PL spectra of perovskite samples were obtained via spectrometer (FLS980) at an emission laser of 510 nm. The TRPL measurements were carried out via the PicoQuant FluoQuant 300. TPV and TPC measurements were done on a home-made system. A white light bias on the sample was generated from an array of diodes. Red light pulse diodes (0.05s square pulse width, 100 ns rise and fall time) controlled by a fast solid-state switch were used as the perturbation source. The transient photocurrent was measured using 20-ohm external series resistance to operate the device in short circuit. Similarly, transient photovoltage was measured using 1 M Ω external series resistance to operate the device in open circuit. The voltage dynamics on the resistors were recorded on a digital oscilloscope (Tektronix MD03032). The perturbation red light source was set to a suitably low level to the white diodes array with light intensity equivalent to 100 mW cm^{-2} of a standard solar simulator.

Stability Test: The complete PSCs could be encapsulated in a N_2 glove box with a cover glass and UV adhesive. The operational stability of the encapsulated cells was measured at 65 °C/85 °C under a white light emitting diode lamp with sixteen-channel thin film photovoltaic maximum power point tracking test system (YH-VMPP-16). To improve the stability of the device, we replaced the Ag electrode with a Cr/Au electrode and used C_{60} as electron transport layer. The thermal stability of the non-encapsulated solar cells was implemented under 85°C thermal pressure and in a N_2 glove box. The PCEs of the devices were periodically obtained under AM 1.5 G simulated sun light illumination in ambient air.

Density Functional Theory (DFT) Calculations: The dipole moments, HOMO, LUMO, and electrostatic potential were performed using the ORCA 6.0.0 at the B3LYP-D3(BJ)/def2-TZVP level [2]. The surface adsorption behaviors of SAM molecules (Me-4PACz and Me-4PACz-Li) on NiO surface were analyzed using a plane wave (PW) basis and the projector-augmented wave (PAW) pseudopotentials, as

implemented in the Vienna Ab initio Simulation Package (VASP) [3]. The adsorption structures of SAM molecules on the crystal surface were constructed following the methods as described in Ref. [4]. The generalized gradient approximation (GGA) with Perdew-Burke-Ernzerhof (PBE) functional was employed for the exchange-correlation potential, and long-range dispersion interactions were corrected using DFT-D3 method [5]. The energy cutoff was set at 520 eV for the wave functions, with convergence thresholds for energy and atomic force were set to 1×10^{-5} eV and 0.02 eV/Å, respectively. Following Ref.[4], Hubbard corrections for Ni were set as $U = 8$ eV and $J = 0.95$ eV. The slab structures of NiO were built by a 3×3 lateral periodicity, exposing the (100) surface to ~25 Å of vacuum to prevent interactions between slab replicas. The binding energy between SAM molecule and NiO slab was calculated as $E_{binding} = E_{system} - E_{SAMs} - E_{slab}$, where E_{system} is the energy of the whole system upon adsorption of SAM molecules, E_{SAMs} and E_{slab} are the energies of isolated SAM molecule and the NiO slab structure, respectively.

Molecular Dynamics (MD) Simulations: The dispersion behavior of Me-4PACz-Li molecules on the NiO substrate was investigated using classical MD simulations in LAMMPS [6], following the methods outlined in Ref.[7,8]. The NiO substrate was generated by the 24×24×3 supercell of NiO, producing a slab model with dimensions of approximately 100×100×12.6 $Å^3$. The SAM layers, with a thickness of 18 Å, were constructed by randomly placing the Me-4PACz and Me-4PACz-Li molecules above the substrate using the Packmol software [9]. The distance between SAM layer and the NiO substrate was maintained at 4.8 Å. The simulation models were created with 6 different fractions of Me-4PACz-Li (*i.e.*, Me-4PACz: Me-4PACz-Li = 1:0, 0.9:0.1, 0.75:0.25, 0.5:0.5, 0.25:0.75, and 0:1), while the total number of SAM molecules was kept at 200. The interactions within SAM molecules were described using the OPLS-AA force field [10], which has been widely used in simulating the aggregation of SAM molecules. The atomic charges of the SAM molecules were determined using the restrained electrostatic potential charges computed from ORCA

6.0.0 at the B3LYP-D3(BJ)/def2-TZVP level [2]. The interactions within NiO substrate were described using the INTERFACE potential [11], which has shown good promise in reproducing the molecular adsorption behavior on various metal oxides. The interactions between SAM molecules and NiO substrate were described by Lennard-Jones potential using the geometric mixing rule. Long-range Coulombic interactions were calculated using the Particle-Particle Particle-Mesh (PPPM) method with an accuracy of 10^{-5}. The simulation models were dynamically equilibrated at 300 K in the canonical ensemble (NVT) for 1 ns. The motion of atoms was described using the velocity Verlet integration with a time step of 1 fs, and periodic boundary condition was applied in all directions. The surface coverage of SAM molecules on the substrate was quantified by constructing a surface mesh using the method implemented in the Ovito software [12], which was also used for visualizing the simulated structures. The interfacial interactions between SAM molecules and NiO substrate were estimated by calculating the adsorption energy as $E_{inter} = E_{total} - E_{SAMs} - E_{NiO}$, where E_{total}, E_{SAMs}, and E_{NiO} are the potential energy of the whole system, SAM molecules, and NiO substrate, respectively. The calculated E_{inter} is normalized by the number of SAM molecules (200).

Supplementary Note 1

The surface coverage of SAM was calculated using the formula

$$\Gamma = \frac{A(\lambda)}{1000\varepsilon(\lambda)} \quad (1)$$

where Γ is the surface coverage (mol cm^{-2}), $A(\lambda)$ is the absorbance of the SAM and $\varepsilon(\lambda)$ is the molar extinction coefficient of SAM molecule [13]. The $\varepsilon(\lambda)$ value of 5.53×10^3 M^{-1} cm^{-1} for Me-4PACz and LiOH-reacted Me-4PACz at their absorption maximum in DMF.

Supplementary Note 2

CV measurements were conducted using a three-electrode configuration. The working electrodes were prepared using a spin coating method on an ITO electrode. The exposed area of the working electrode to the electrolyte measures 15 mm × 12 mm. A platinum plate and an Ag/AgCl electrode (in a 3.0 M KCl solution) were employed

as the counter and reference electrodes, respectively. The measurements were performed in an Ar-saturated solution of 1,2-dichlorobenzene (o-DCB) with 0.1 M tetrabutylammonium hexafluorophosphate ($TBA^+PF_6^-$) serving as the supporting electrolyte. All potentials are referenced against the ferrocene redox couple, serving as an internal standard. The effective coverage of the SAMs on the ITO surface is measured by the slope of a linear dependency of the oxidative peak intensity against the scan rate as follows：

$$i_{p,o} = \frac{n^2F^2}{4RTN_A} A\ \Gamma^*\ v \tag{2}$$

$i_{p,o}$ is the oxidative peak current, v is the voltage scan rate, n is the number of electrons transferred, F is the Faraday constant (96485.33 C mol^{-1}), R is the universal gas constant (8.314 J K^{-1} mol^{-1}), T is the temperature, N_A is the Avogadro constant, A is the electrode area, and Γ* is the areal density.

Supplementary Note 3

Change the φ (where φ is the angle of the diffraction vector with respect to the sample's normal direction) from 10° to 50° to get the relationship between the interplanar distance d_n and $Sin^2φ$. The residual stress in the perovskite film is estimated based on the slope of the d_n-$Sin^2φ$ fitting curve given by:

$$\sigma_R = (\frac{E}{1+v})(\frac{m}{d_n}) \tag{3}$$

where σ_R is the residual stress of the film; E is the Young's modulus of the perovskite film (15 GPa); v is the Poisson's ratio (0.3); m is the slope of the straight line after linear fitting; d_n is the intercept of the straight line after linear fitting.[14] ↵

Supplementary Note 4

We fabricated hole-only devices (ITO/NiO_x-NPs/Me-4PACz or LiOH-reacted Me-4PACz/perovskite film /PTAA /Ag) and evaluated the effect of LiOH-reacted Me-4PACz on defect state density and carrier mobility using the space charge limited

current (SCLC) method. The low-bias region is the ohmic region, the middle-bias region is the defect filling limit region, and the high-bias region is the SCLC region. The defect filling limit voltage (V_{TFL}) is determined at the junction of the low and middle bias regions, and the defect density (N_t) is obtained using Eq. 4:[15]

$$N_t = \frac{2\varepsilon\varepsilon_0 V_{TFL}}{eL^2} \quad (4)$$

where ε_0 and ε are the vacuum and relative permittivity, e is the electron charge, and L is the film thickness.

According to the Mott-Gurney law in Eq. 5, the carrier mobility (μ) can be calculated from the Child region:[16]

$$\mu = \frac{8}{9}\frac{J}{\varepsilon\varepsilon_0}\frac{L^3}{V^2} \quad (5)$$

Supplementary Note 5

The hysteresis factor (HF) is quantified as:

$$HF = \frac{PCE_{reverse} - PCE_{forward}}{PCE_{reverse}} \quad (6)$$

Supplementary Note 6

The carrier recombination mechanism was determined by studying the dependence of V_{OC} of PSCs on the incident light intensity (I) using Eq. 7:

$$V_{OC} = \frac{nk_BT}{q} ln(I) \quad (7)$$

where n is the ideality factor, k_B is the Boltzmann constant, and T is the temperature.

Supplementary Note 7

Admittance spectroscopy (AS) [17]

AS is an effective technique for estimating both the energy level of trap states and the distribution of trap state density, which has been extensively applied to many photovoltaic systems, such as organic solar cells, Cu_2ZnSnS_4 solar cells, and PSCs. As the literature reported, for a p-type perovskite semiconductor, the defect activation energy (Ea) is approximately the depth of the trap state energy level (E_T) relative to the

valence band maximum (VBM) energy level (E_{VBM}) of perovskite ($Ea= E_T - E_{VBM}$). Ea and the characteristic transition angular frequency (ω_0) can be expressed in the relation $\omega_0 = \beta T^2 \, exp(-\frac{E_a}{k_B T})$, where β is a a temperature dependent parameter, T is the temperature and k_B is the Boltzmann's constant. The ω_0 is determined by the derivative of the capacitance−frequency spectrum. According to this equation, the Arrhenius plot ($ln(\frac{\omega_0}{T^2}) = ln\,\beta - \frac{E_a}{k_B T}$), and the value of Ea can be obtained from the slope of the Arrhenius plot line. The distribution of trap state density can be derived from the equation, $N_T(E_\omega) = -\frac{V_{bi}}{qW}\frac{dC}{d\omega}\frac{\omega}{k_B T}$, $E_\omega = k_B T \, ln(\frac{\omega_0}{\omega})$, where V_{bi} is the built-in potential, W is the depletion width, q is the elementary charge, C is the capacitance, and ω is the applied angular frequency. V_{bi} and W can be extracted from the Mott−Schottky analysis through the capacitance-voltage measurement. According to the depletion approximation, the C, V_{bi}, and W at the junction can be expressed in the relation, $\frac{C}{A} = \frac{\varepsilon\varepsilon_0 N}{W} = \sqrt{\frac{q\varepsilon\varepsilon_0 N}{2(V_{bi}-V)}}$, where A is active area, ε is the static permittivity of perovskite, ε_0 is the permittivity of free space, N is the apparent doping profile in the depleted layer, and V is the applied bias. A Mott-Schottky plot ($\frac{A^2}{C^2} = \frac{2(V_{bi}-V)}{q\varepsilon\varepsilon_0 N}$) describes a straight line where the intersection on the bias axis determines V_{bi} and the slope gives the impurity doping density N. Then, the depletion width $W = \sqrt{\frac{2\varepsilon\varepsilon_0 V_{bi}}{qN}}$corresponding to the zero bias can be calculated.

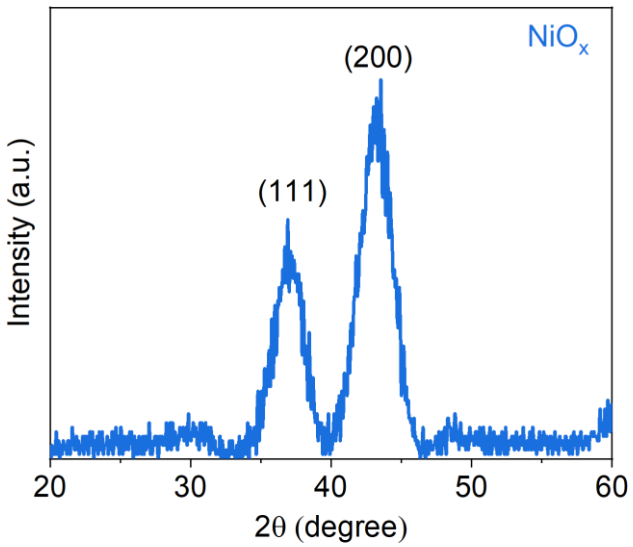

Supplementary Fig. 1 | The XRD pattern of NiO_x-NPs.

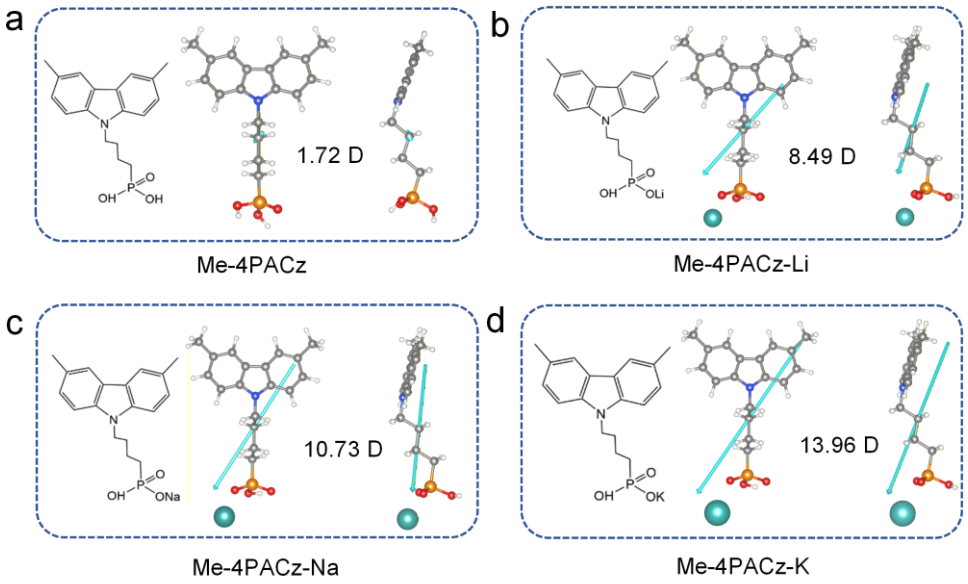

Supplementary Fig. 2 | Structures and dipole moments of SAM molecules. Molecular structures and calculated dipole moments (μ) of (**a**) Me-4PACz, (**b**) Me-4PACz-Li, (**c**) Me-4PACz-Na, and (**d**) Me-4PACz-K.

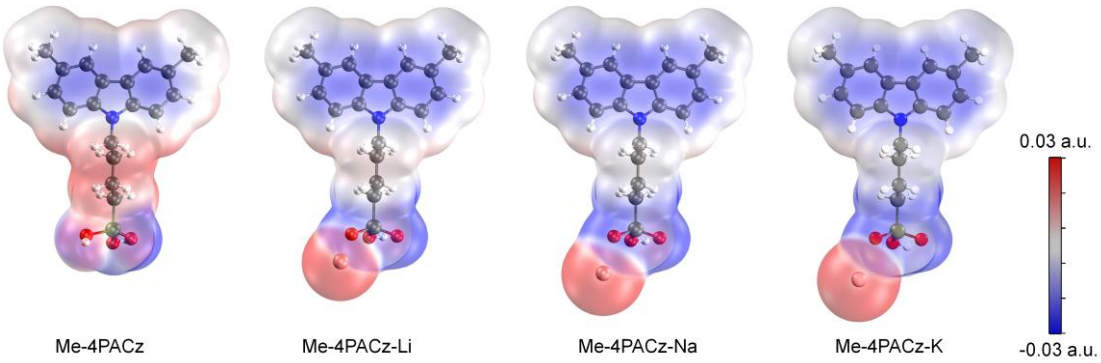

Supplementary Fig. 3 | Calculated electrostatic potential of SAMs. Electrostatic potential (ESP) distribution of Me-4PACz, Me-4PACz-Li, Me-4PACz-Na, and Me-4PACz-K molecules from DFT calculations, where the blue and red clouds represent the electron-rich and electron-poor regions, respectively.

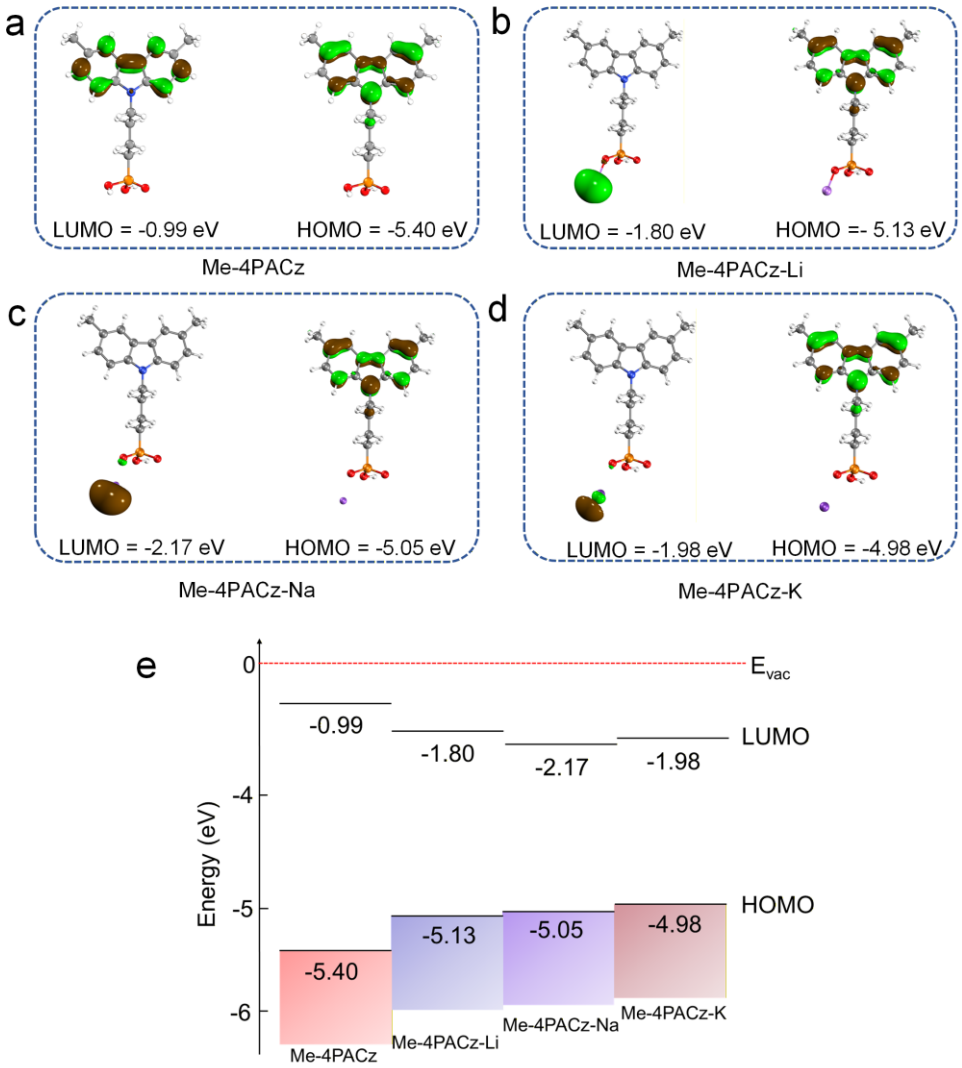

Supplementary Fig. 4 | Calculated energy levels of SAM molecules. Calculated LUMO and HOMO of (**a**) Me-4PACz, (**b**) Me-4PACz-Li, (**c**) Me-4PACz-Na, and (**d**) Me-4PACz-K. (**e**) Energy alignment of SAMs based on the calculated HOMO and LUMO levels.

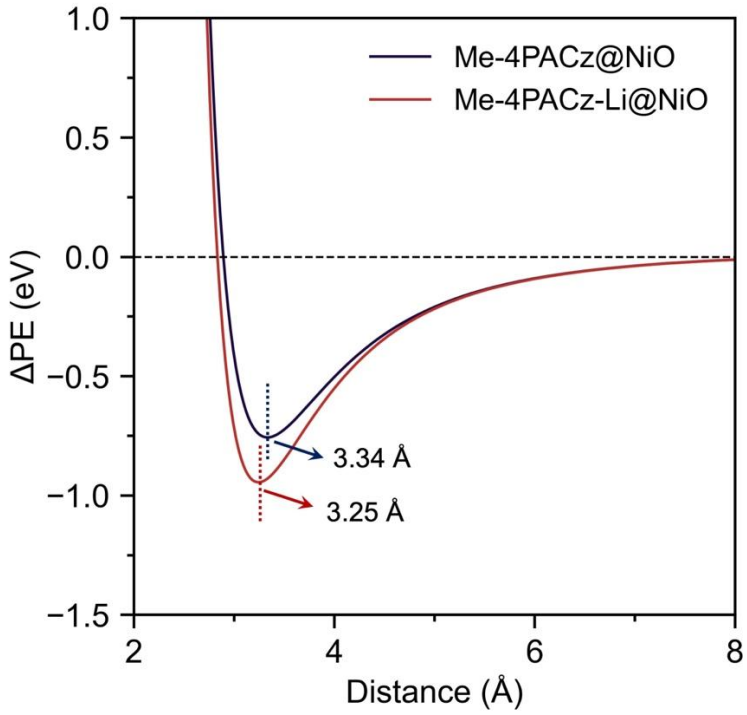

Supplementary Fig. 5 | Potential energy curves between SAM molecule and NiO substrate. The change in potential energy (ΔPE) for the two systems as a function of the distance in the z-direction between SAM molecule and NiO substrate. The distance is represented by the height of P atom relative to the NiO surface.

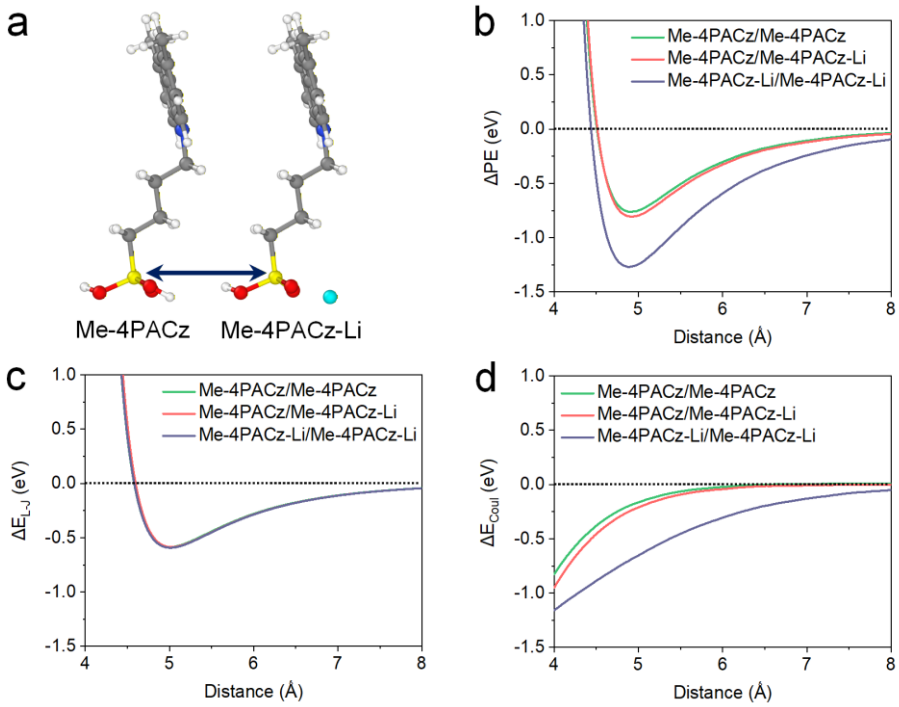

Supplementary Fig. 6 | Interactions between two SAM molecules as a function of the intermolecular distance, defined as the separation between two P atoms. (**a**) Schematic representation of the two SAM molecules. (**b**) Potential energy (ΔPE), and (**c–d**) the contributions from (**c**) Lennard-Jones and (**d**) Coulomb interactions.

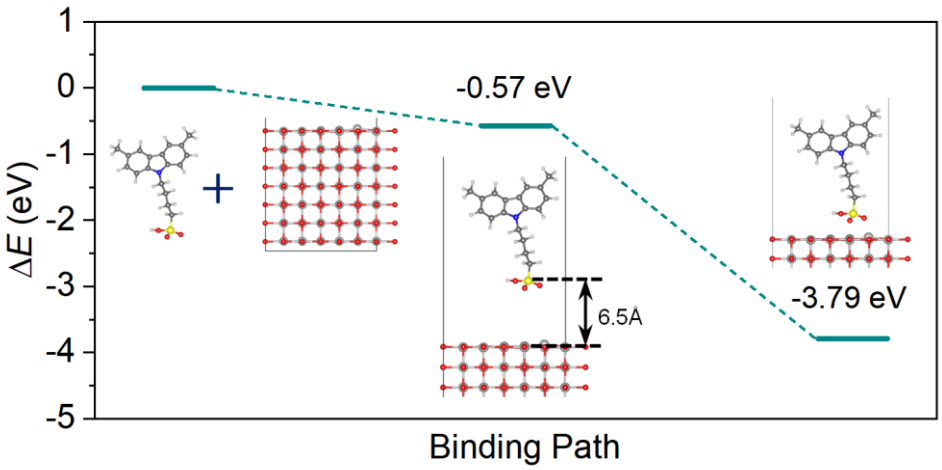

Supplementary Fig. 7 | Calculated potential energy of Me-4PACz⁻ on a NiO (100) surface with different distances. Change of potential energy along the binding path for Me-4PACz⁻ on the NiO (100) surface, obtained at GGA/PBE+U level with long-range dispersion interactions.

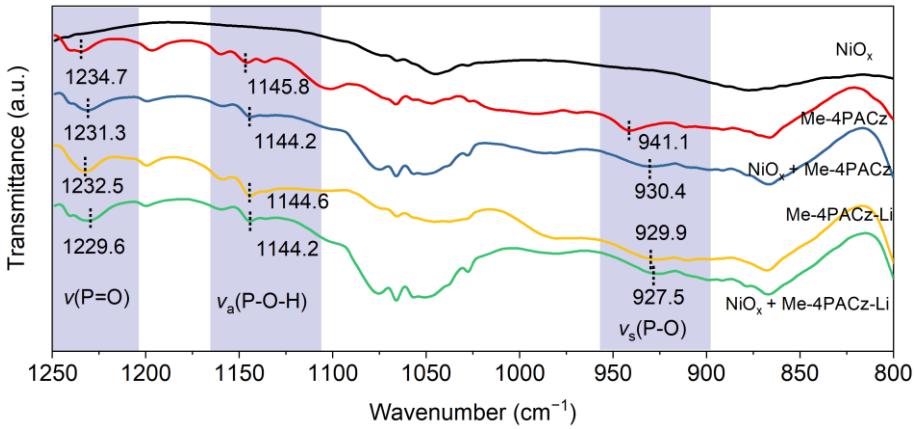

Supplementary Fig. 8 | FTIR characterization. FTIR spectra of NiO_x-NPs, Me-4PACz, Me-4PACz+NiO_x-NPs, Me-4PACz-Li, and Me-4PACz-Li+NiO_x-NPs films.

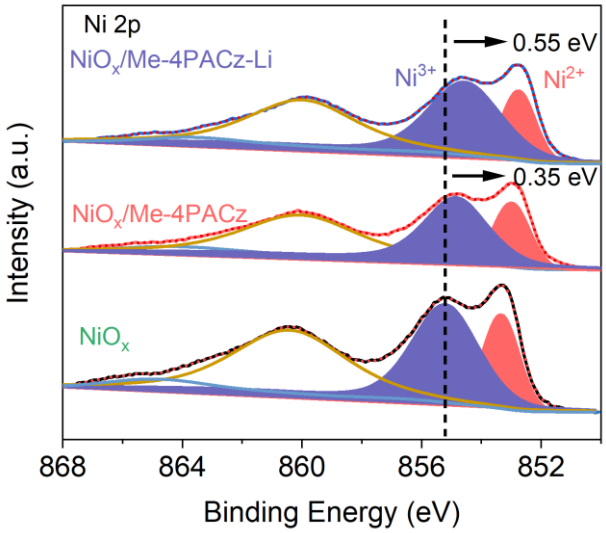

Supplementary Fig. 9 | XPS characterization. XPS spectra of Ni 2*p* for NiO_x-NPs, NiO_x-NPs/Me-4PACz, and NiO_x-NPs/Me-4PACz-Li films.

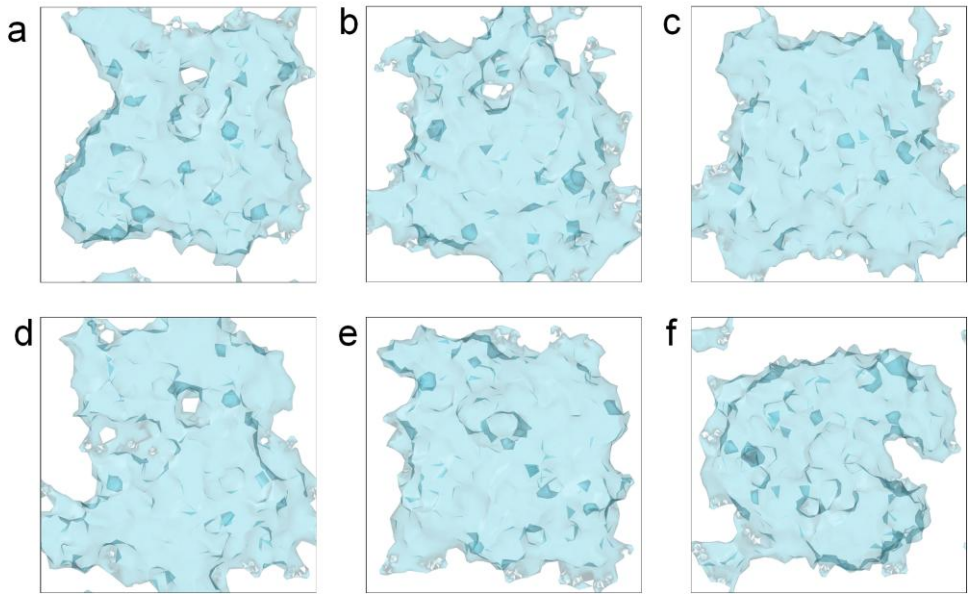

Supplementary Fig. 10 | Simulation of the coverage of different SAM molecules on NiO surfaces. Surface coverage of different SAM layers, including (**a**) pure Me-4PACz, (**b**) 90% Me-4PACz and 10% Me-4PACz-Li, (**c**) 75% Me-4PACz and 25% Me-4PACz-Li, (**d**) 50% Me-4PACz and 50% Me-4PACz-Li, (**e**) 25% Me-4PACz and 75% Me-4PACz-Li, and (**f**) pure Me-4PACz-Li on the NiO (100) substrate after 1 ns MD simulation (The size of the slab model is 10 nm x10 nm).

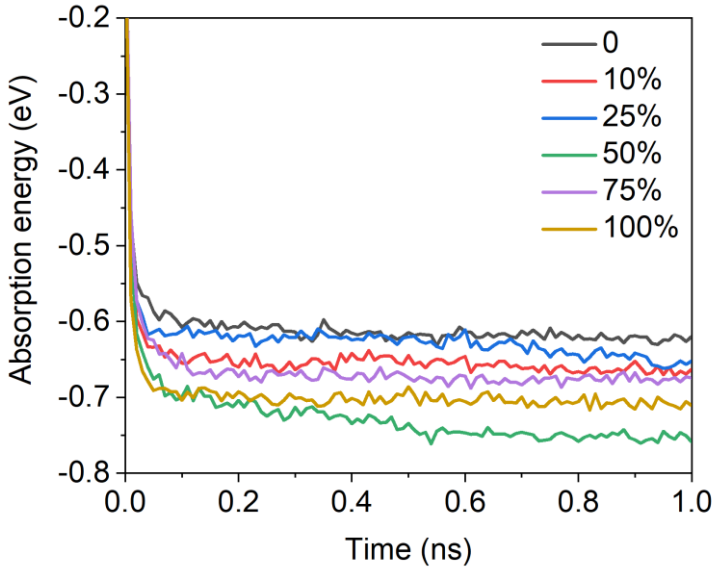

Supplementary Fig. 11 | Calculated adsorption energies of LiOH-reacted SAM molecules with different reaction ratios on NiO (100) surface over simulation time.

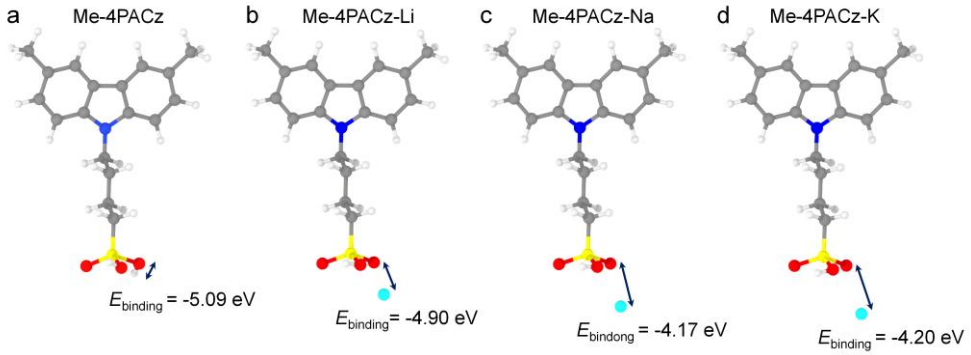

Supplementary Fig. 12 | The binding energies between H/alkali metal atoms and O atoms in the phosphate groups. Structures and corresponding binding energies between H/alkali metal atoms and O atoms in the phosphate groups of (**a**) Me-4PACz, (**b**) Me-4PACz-Li, (**c**) Me-4PACz-Na, and (**d**) Me-4PACz-K.

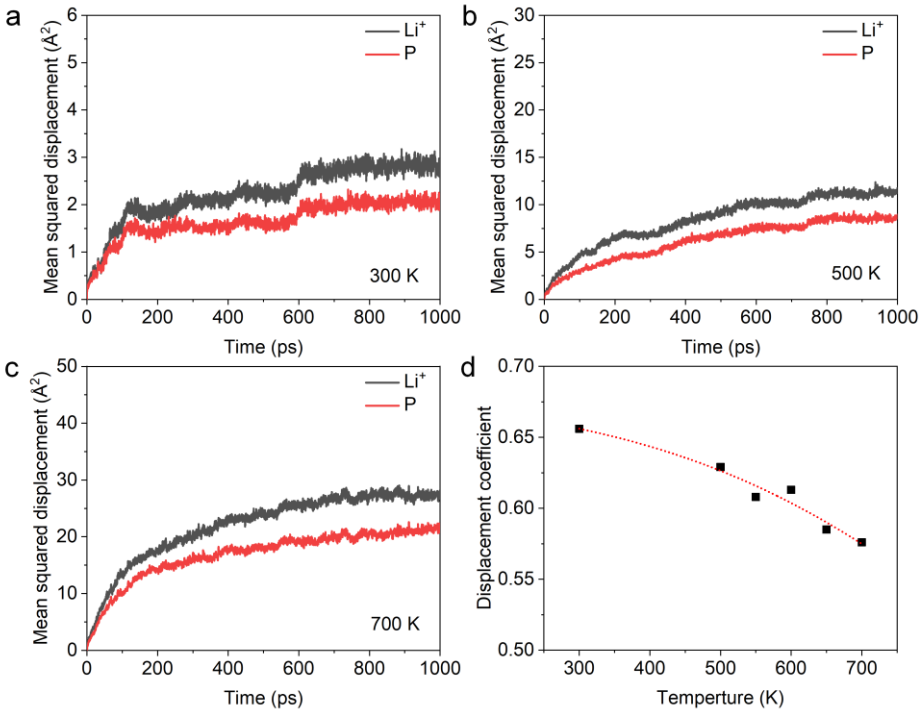

Supplementary Fig. 13 | Diffusion behavior of Li^+ and P within Me-4PACz-Li. Mean squared displacement of Li^+ and P at different temperatures: (**a**) 300 K, (**b**) 500 K, and (**c**) 700 K. (**d**) Displacement coefficient $C(t)$ between Li^+ and P as a function of temperatures. A value of $C(t)$=1 indicates that Li and P move in the same direction, $C(t)$ = -1 indicates motion in opposite directions, and $C(t)$=0 corresponds to the absence of correlation.

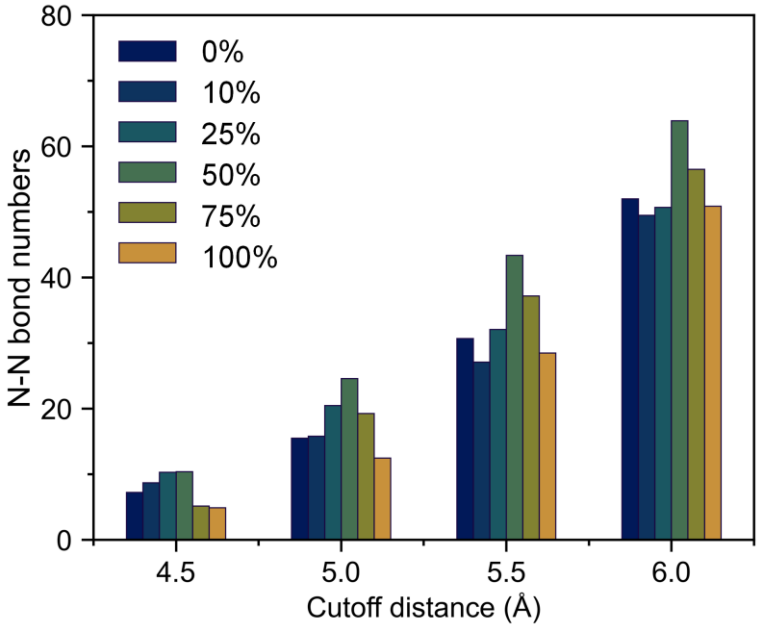

Supplementary Fig. 14 | The distribution of distances between neighboring SAM molecules to identify the compactness. The number of neighboring molecules with various distances within SAM layers adsorbed on NiO substrates after a 1 ns MD simulation. Li-Me shows the largest number of neighboring molecules with small distance, indicating the highest compactness of the SAM layer.

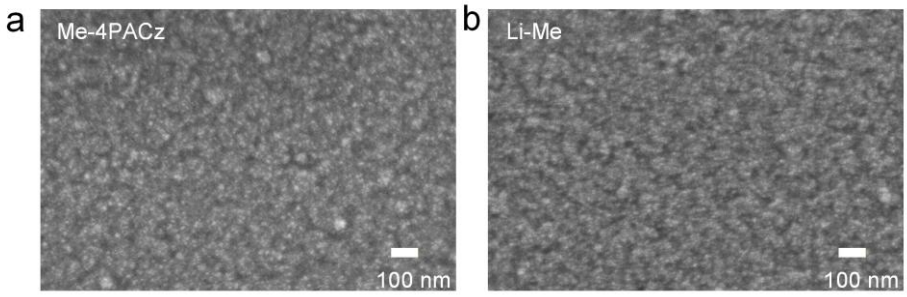

Supplementary Fig. 15 | SEM characterization of SAM layers coated on NiO_x-NPs films. Top-view SEM images of (**a**) Me-4PACz and (**b**) Li-Me on NiO_x-NPs films.

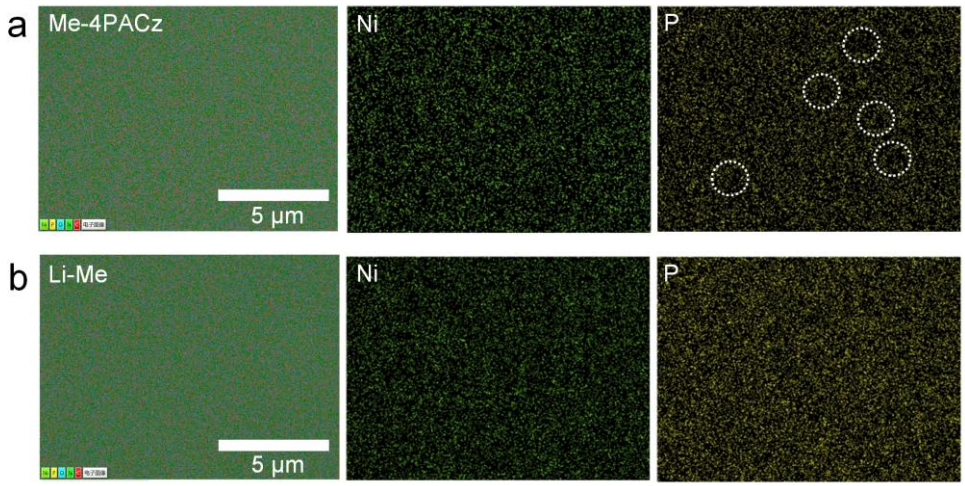

Supplementary Fig. 16 | Elemental mapping of SAM layers coated on NiO_x-NPs films under SEM. Elemental mapping of Ni and P for (**a**) Me-4PACz and (**b**) Li-Me modified NiO_x-NPs. The while circles indicate the areas with low density of P.

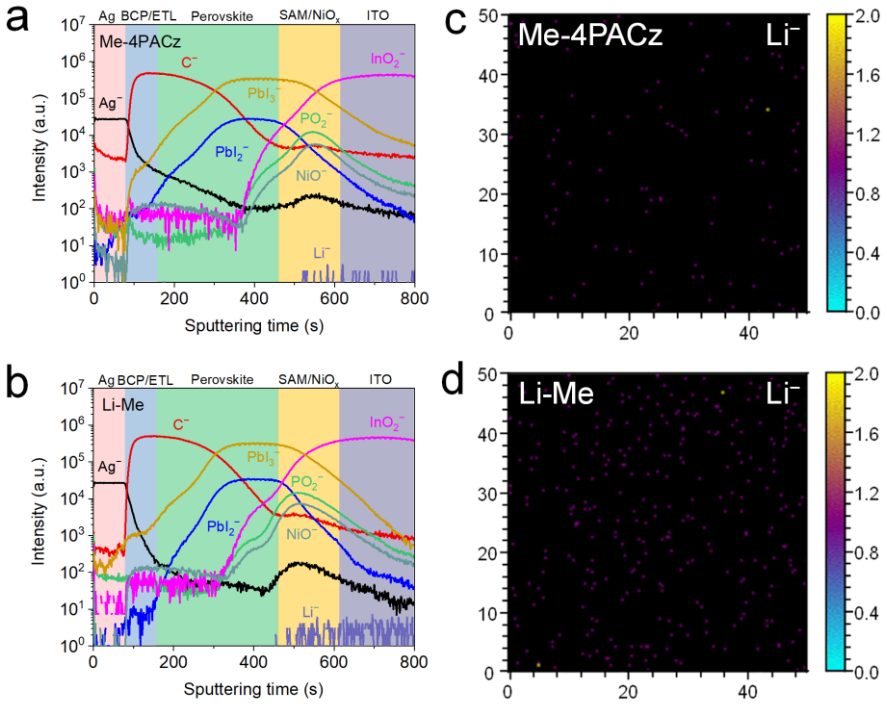

Supplementary Fig. 17 | Element distribution characterized by TOF-SIMS. (**a-b**) ToF-SIMS depth profiles of PSC devices based on Me-4PACz/NiO_x-NPs and Li-Me/NiO_x-NPs. TOF-SIMS signal mapping of (**c-d**) Li^- of the device based on Me-4PACz and Li-Me (the range is 50×50 μm).

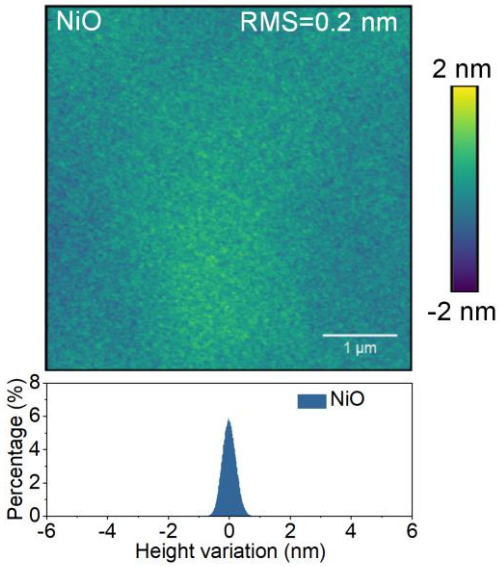

Supplementary Fig. 18 | AFM morphology images and highly statistical distribution of NiO (RMS: root mean square).

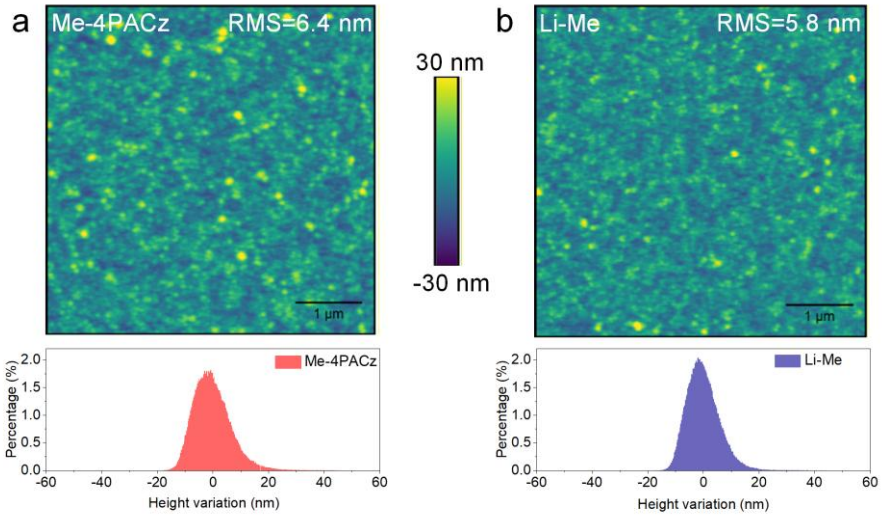

Supplementary Fig. 19 | AFM characterization of SAM layers coated on NiO_x-NPs films. AFM morphology images and highly statistical distribution of (**a**) Me-4PACz and (**b**) Li-Me on NiO_x-NPs (RMS: root mean square).

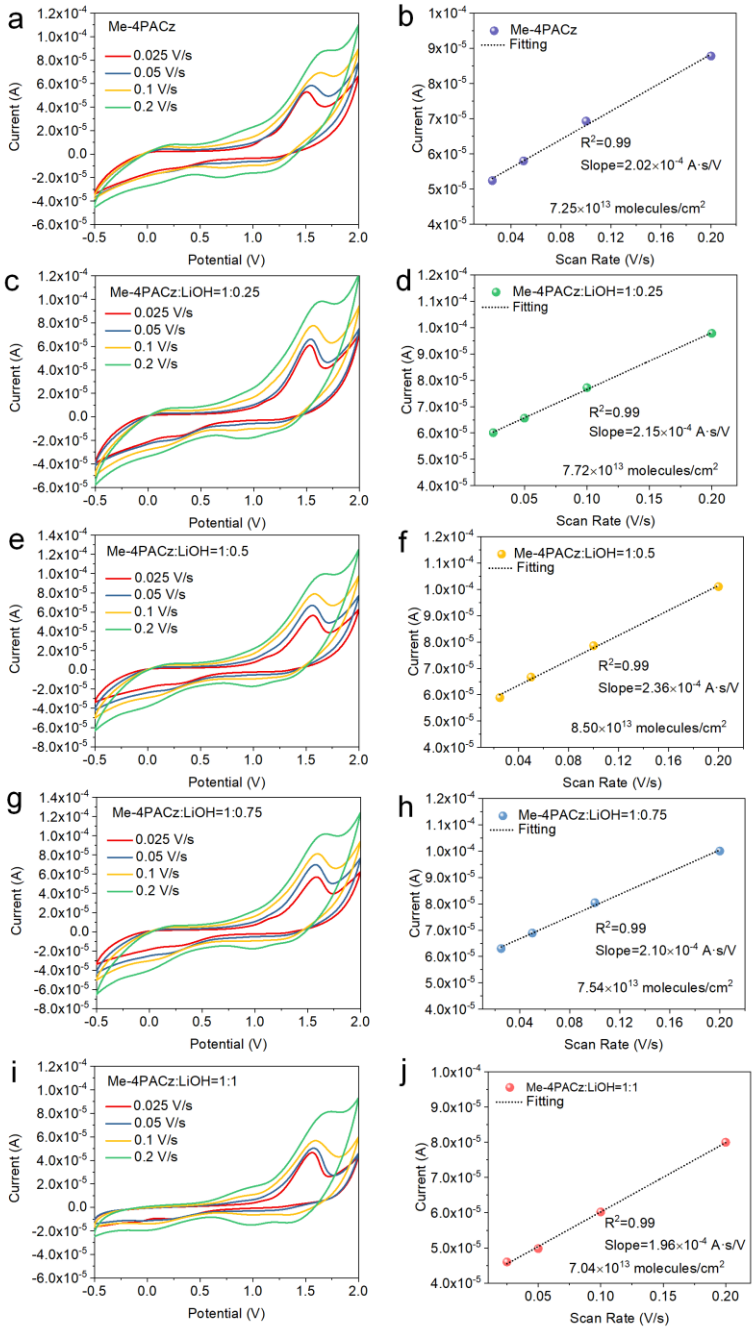

Supplementary Fig. 20 | Cyclic voltammetry (CV) characterization of SAM layers coated on NiO_x-NPs films. Cyclic voltammograms of (**a**) ITO/NiO_x-NPs/Me-4PACz, (**c**) ITO/NiO_x-NPs/Me-4PACz:LiOH=1:0.25, (**e**) ITO/NiO_x-NPs/Me-4PACz:LiOH=1:0.5, (**g**) ITO/NiO_x-NPs/Me-4PACz:LiOH=1:0.75, and (**i**) ITO/NiO_x-NPs/Me-4PACz:LiOH=1:1 as the working electrode measured in Ar-saturated o-DCB solution under different voltage scan rates. The relationship between the oxidative peak current and the voltage scan rate for (**b**) ITO/NiO_x-NPs/Me-4PACz, (**d**) ITO/NiO_x-NPs/Me-4PACz:LiOH=1:0.25, (**f**) ITO/NiO_x-NPs/Me-4PACz:LiOH=1:0.5, (**h**) ITO/NiO_x-NPs/Me-4PACz:LiOH=1:0.75, and (**j**) ITO/NiO_x-NPs/Me-4PACz:LiOH=1:1 samples. The dashed line represents a linear fit to the raw data.

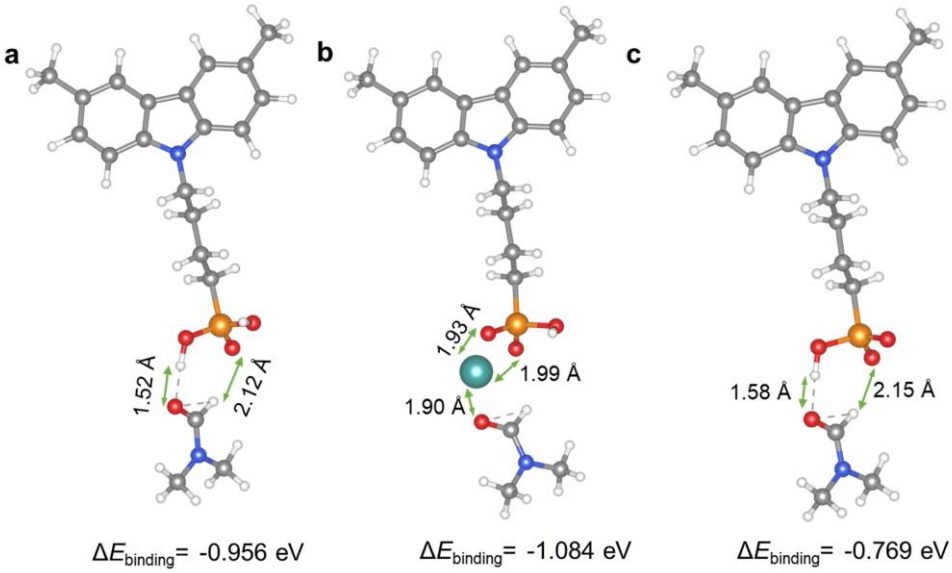

Supplementary Fig. 21 | Binding energy between SAM and DMF molecules. Optimized structure and the calculated bind energy ($\Delta E_{binding}$) for (**a**) DMF/Me-4PACz, (**b**) DMF/Me-4PACz-Li, and (**c**) DMF/Me-4PACz^{-}.

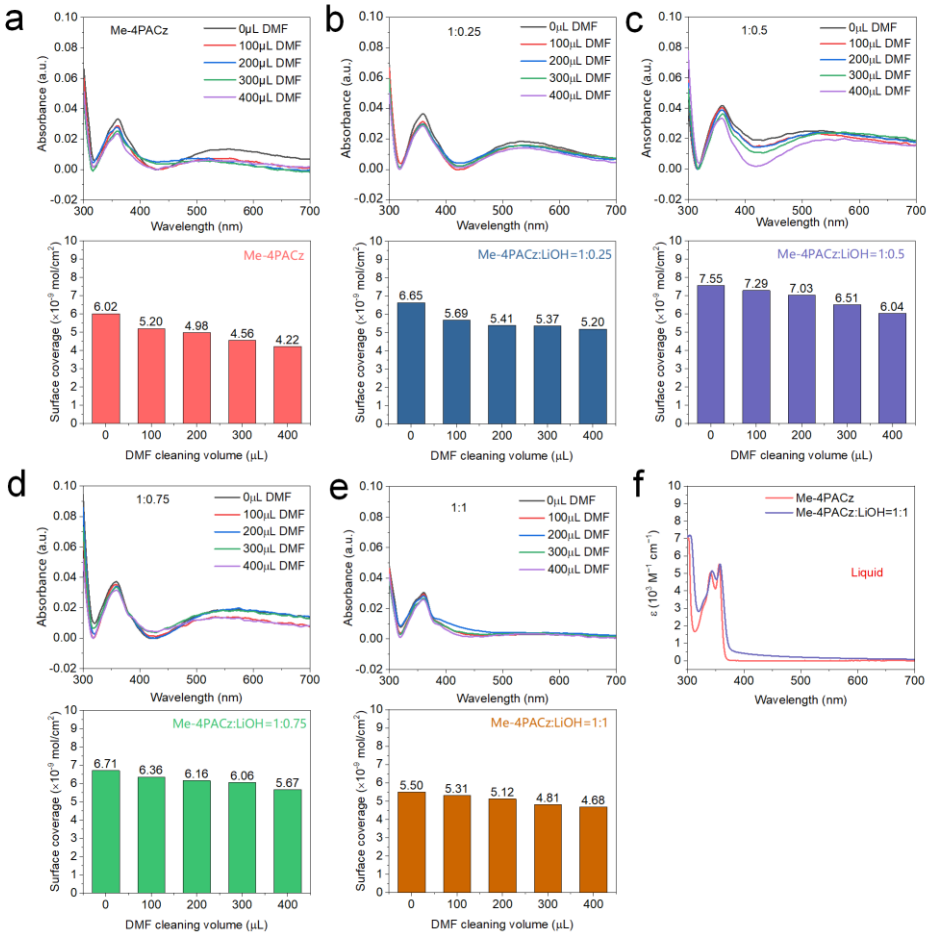

Supplementary Fig. 22 | Changes in the surface coverages of SAMs after DMF washing. (**a-e**) Top: UV-Vis absorption spectra of different SAMs on NiO_x-NPs films after annealing and then being washed with different amounts of DMF. The absorbance of NiO_x-NPs was subtracted by using a similar NiO_x-NPs substrate. Bottom: SAM density on NiO_x-NPs as a function of DMF washing volume. (**f**) UV-visible absorption spectra of SAMs (Me-4PACz and Me-4PACz-Li) dissolved in DMF with a concentration of 10^{-5} M.

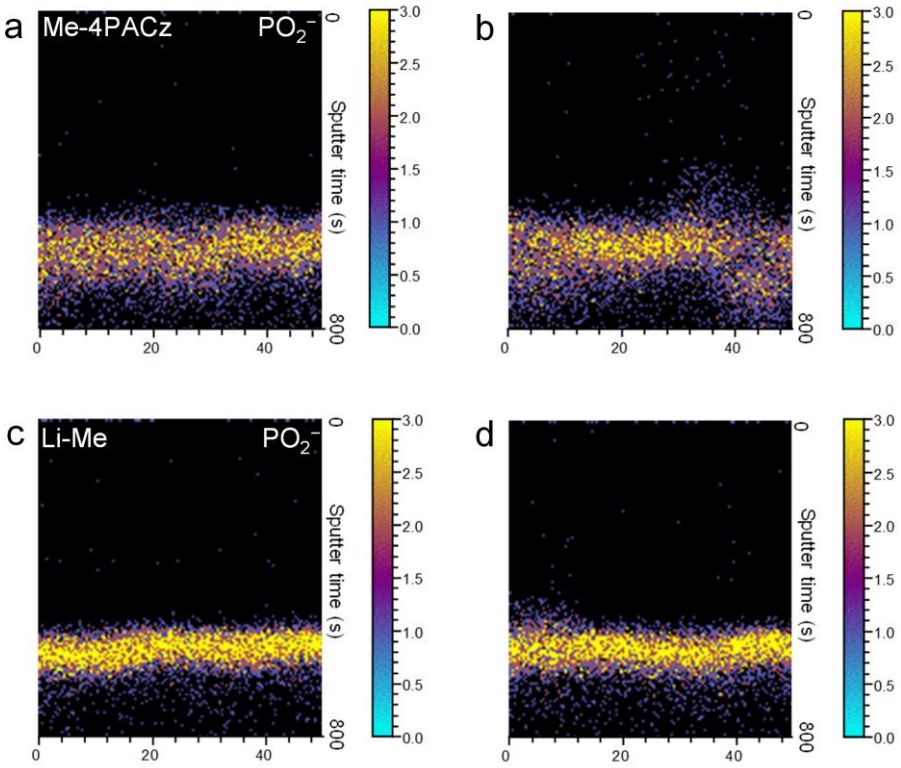

Supplementary Fig. 23 | Distribution of SAMs characterized by TOF-SIMS. (**a-b**) Cross-sectional TOF-SIMS mapping of Me-4PACz (PO_2^-) in initial and aged PSCs (300 h at 85 °C), respectively. (**c-d**) Cross-sectional TOF-SIMS mapping of Li-Me (PO_2^-) in initial and aged PSCs (300 h at 85 °C), respectively (the range is 50 μm).

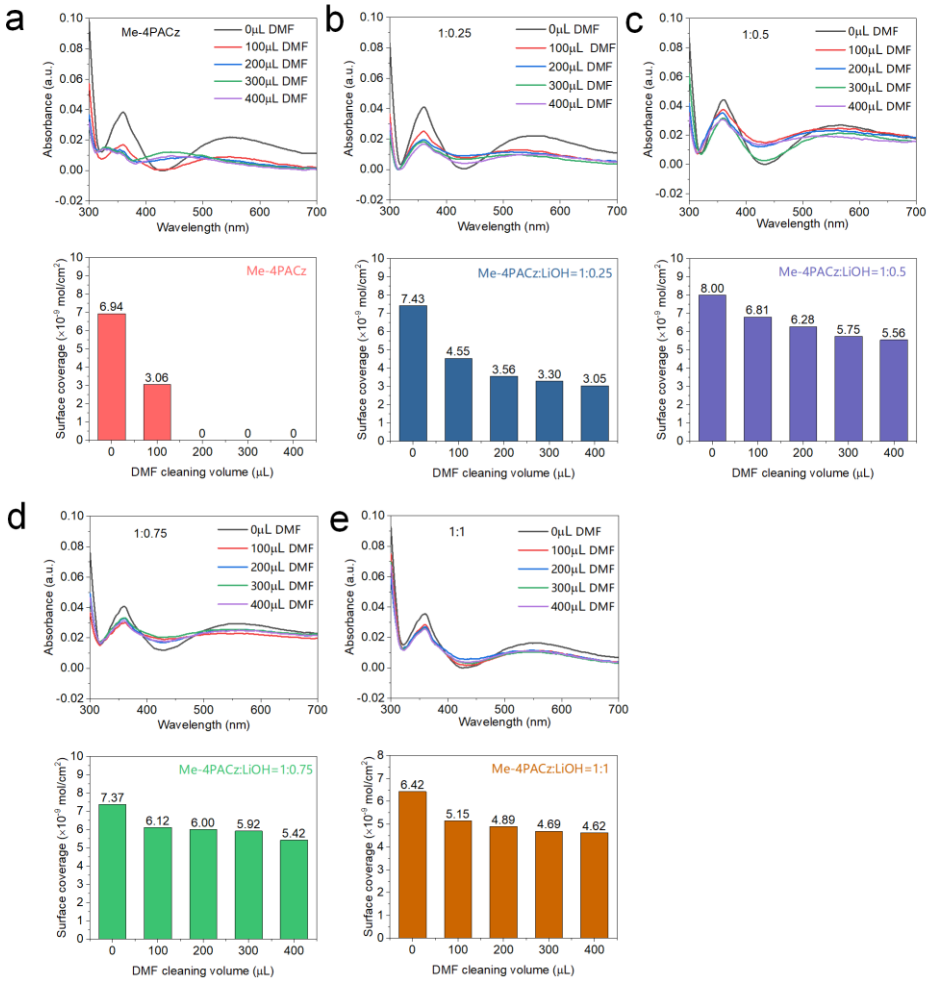

Supplementary Fig. 24 | Changes in the surface coverages of SAMs after DMF washing. (**a-e**) Top: UV-Vis absorption spectra of SAMs on NiO_x-NPs without annealing and being washed with different amounts of DMF. Bottom: Variation in SAM densities on NiO_x-NPs as a function of DMF washing volume.

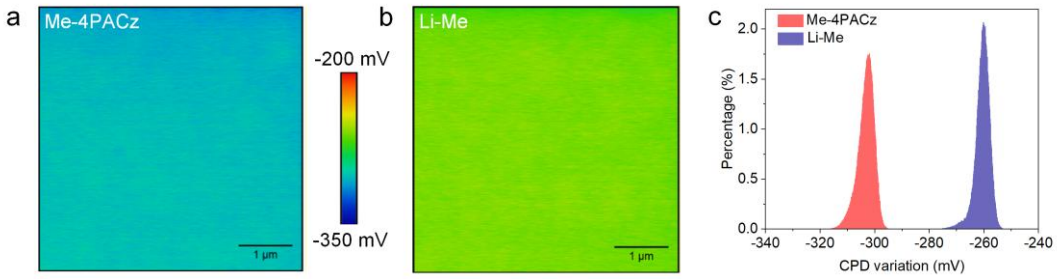

Supplementary Fig. 25 | KPFM characterization of SAM layers. KPFM images of (**a**) NiO_x-NPs/Me-4PACz and (**b**) NiO_x-NPs/Li-Me. (**c**) Potential statistical distribution in KPEM.

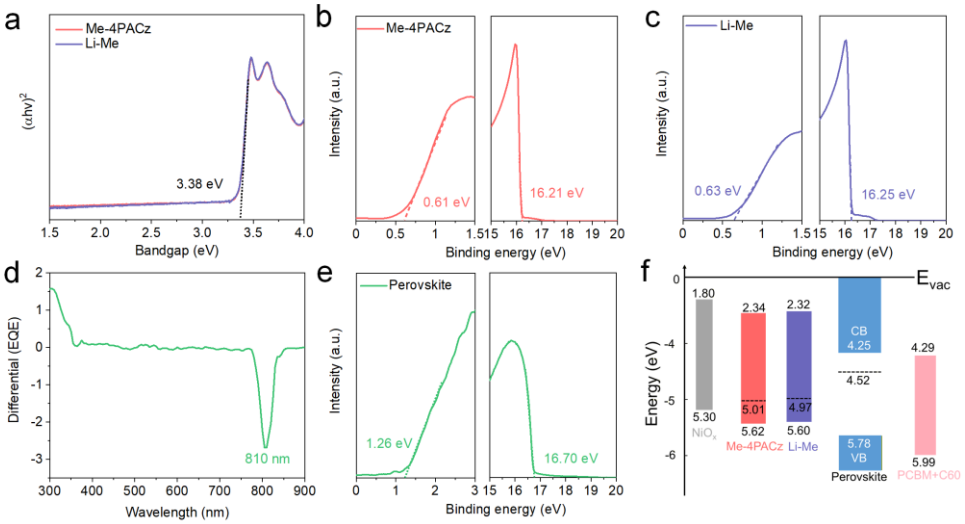

Supplementary Fig. 26 | The characterization of energy levels of SAMs. (**a**) Tauc-plot curves of Me-4PACz and Li-Me ethanol solutions. UPS data of (**b**) NiO_x-NPs/Me-4PACz and (**c**) NiO_x-NPs/Li-Me. (**d**) d(EQE)/dE versus wavelength confirming the bandgap. (**e**) UPS data of perovskite film. (**f**) Functional layer band structure (E_{vac}, vacuum level; CB, conduction band; VB, valence band).

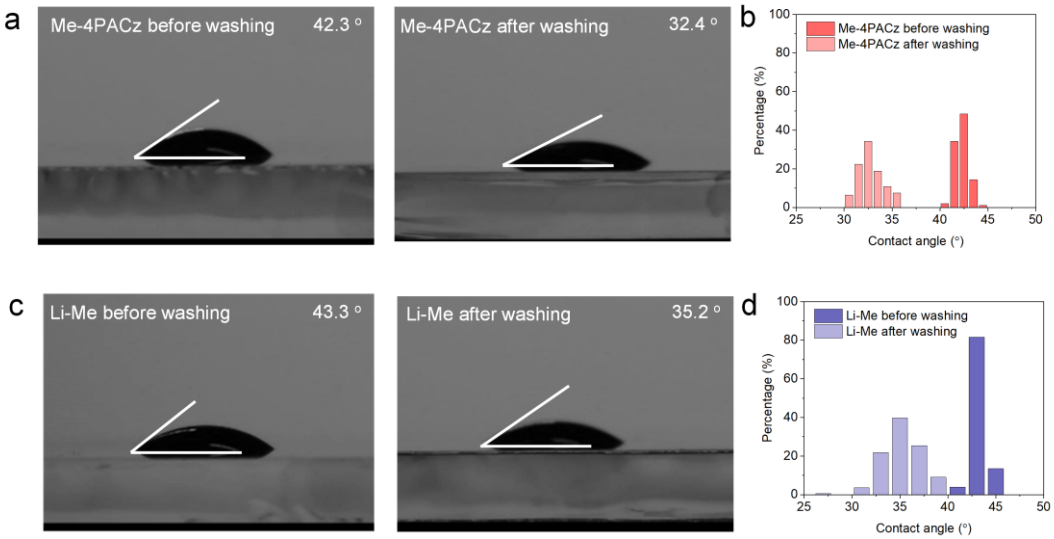

Supplementary Fig. 27 | The contact angle of a perovskite precursor on different SAM surfaces. (**a**) Me-4PACz/NiO_x-NPs and (**c**) Li-Me/NiO_x-NPs. Statistical analysis of contact angles on the surfaces of (**b**) Me-4PACz/NiO_x-NPs and (**d**) Li-Me/NiO_x-NPs.

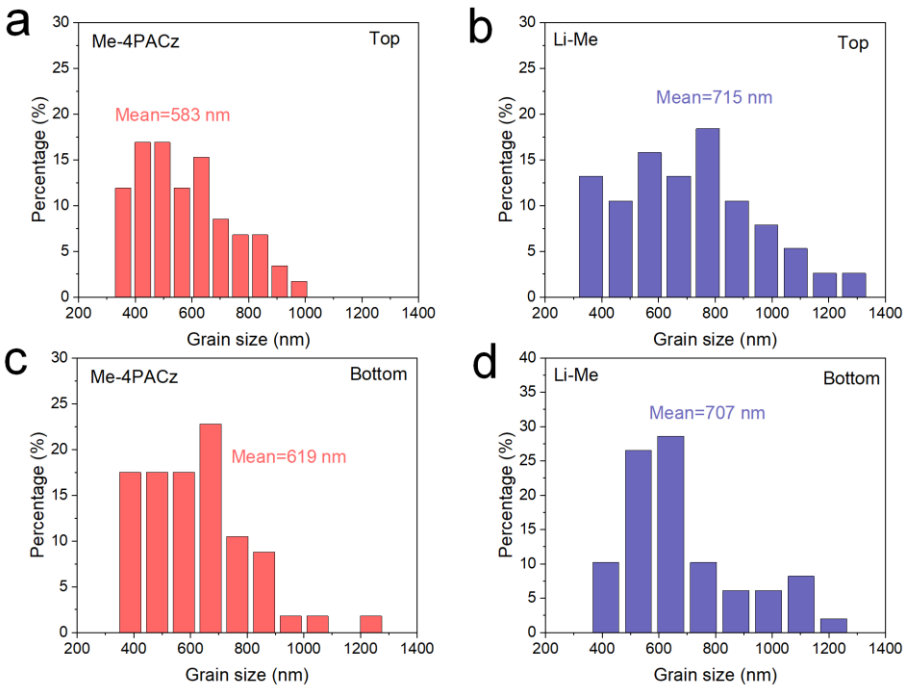

Supplementary Fig. 28 | Statistical distribution of perovskite grain sizes. Histogram distribution of (**a-b**) surface and (**c-d**) bottom perovskite films on Me-4PACz/NiO_x-NPs and Li-Me/NiO_x-NPs layers.

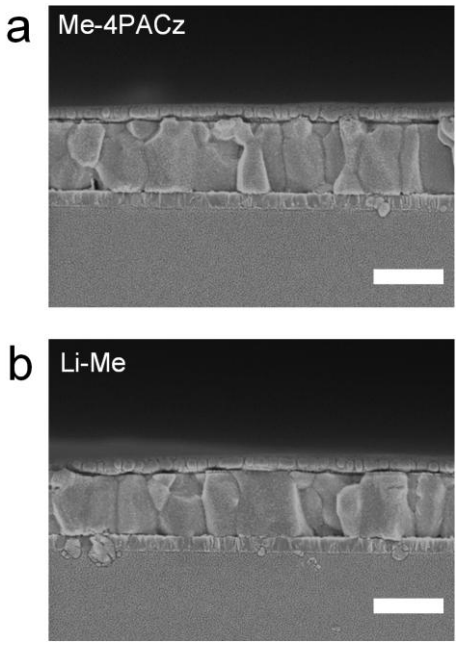

Supplementary Fig. 29 | Cross-sectional SEM. (a-b) Cross-sectional views of devices on two different SAMs. The scales in all images are 1 μm.

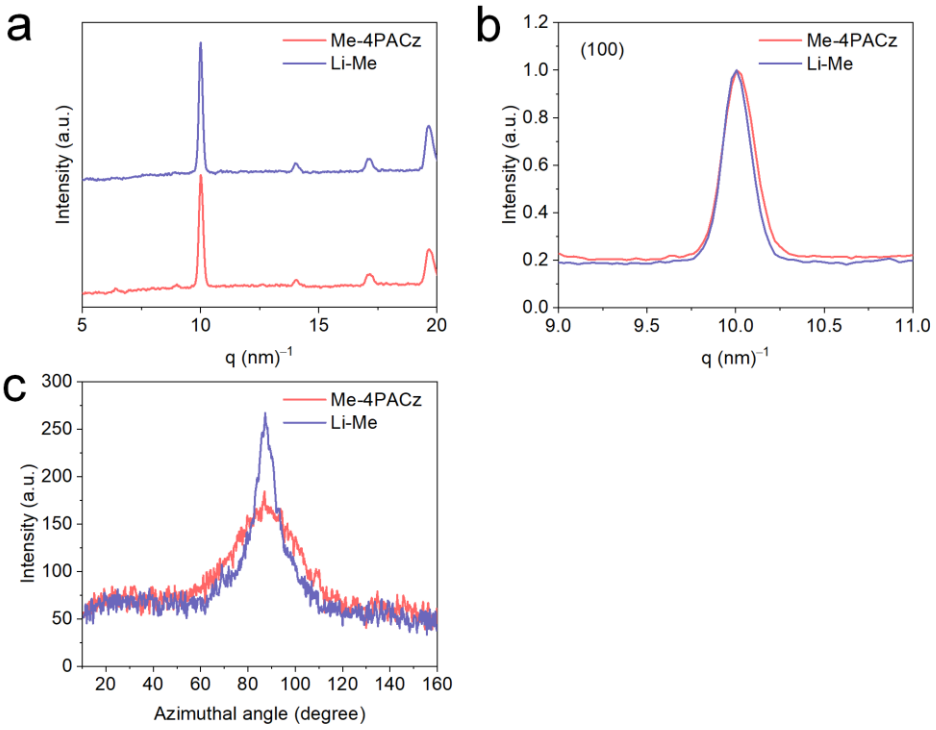

Supplementary Fig. 30 | Crystal orientation analysis of perovskite films. (**a**) Circular average diffraction pattern of perovskite films deposited on Me-4PACz/NiO_x-NPs and Li-Me/NiO_x-NPs. (**b**) The full width at half maximum (FWHM) of the (100) peak. (**c**) Radially integrated intensity plots along the ring at q = 10 nm^{-1}, assigned to the (100) plane of the perovskite films on Me-4PACz/NiO_x-NPs and Li-Me/NiO_x-NPs.

The crystallinity of perovskite films was evaluated by GIWAXS. The diffraction ring in GIWAXS at q values of 10 nm^{-1} corresponds to (100) plane of perovskite. The half-peak width of the (100) plane of the Li-Me based perovskite film is narrower than that of the Me-4PACz based film, indicating enhanced perovskite crystallinity (**Supplementary Fig. 30a-b**). Moreover, The Debye-Scherrer rings of the (100) plane of Li-Me based perovskite film shows sharper diffraction signals, suggesting that the crystal packing is better oriented with a dominant out-of-plane orientation (**Supplementary Fig. 30c**)

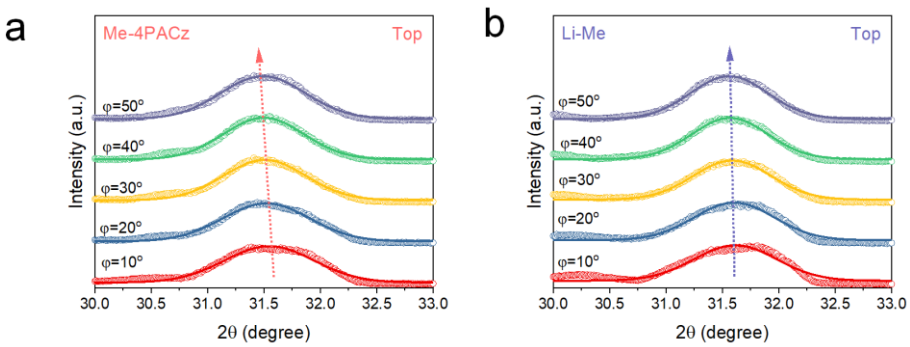

Supplementary Fig. 31 | GIXRD characterization of perovskite films. GIXRD with different φ angles (10°-50°) for perovskite films deposited on (**a**) Me-4PACz/NiO_x-NPs and (**b**) Li-Me/NiO_x-NPs.

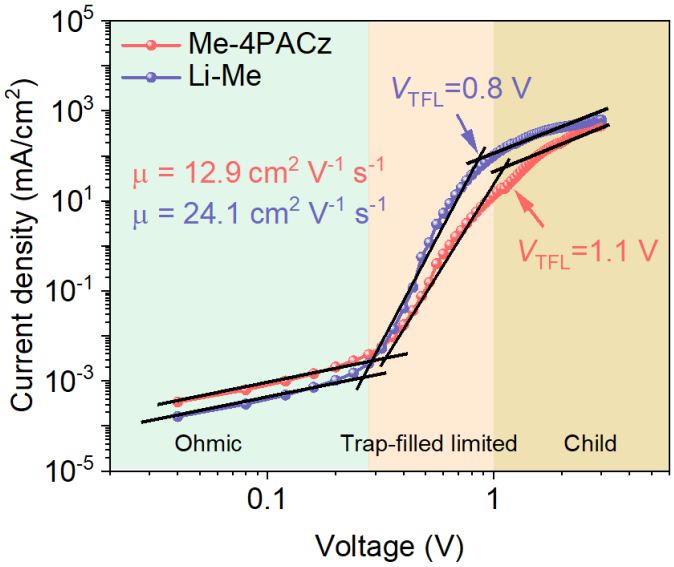

Supplementary Fig. 32 | SCLC of the hole-only perovskite devices prepared on different SAM layers.

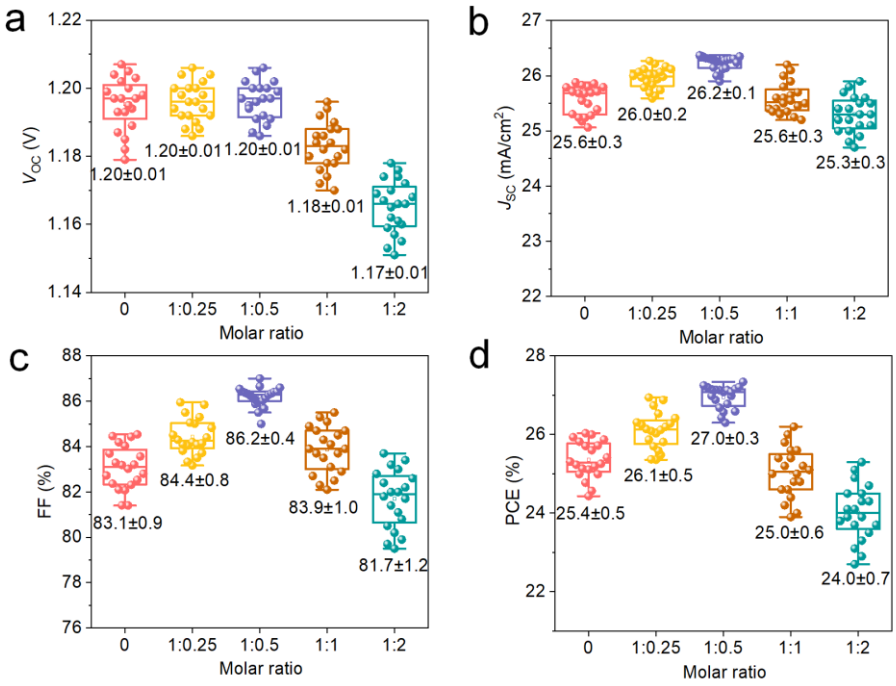

Supplementary Fig. 33 | Statistics of photovoltaic parameters of PSCs. (a-d) Photovoltaic parameters distribution of V_{OC}, J_{SC}, FF, and PCE obtained from 20 devices with various molar ratio of LiOH-reacted Me-4PACz.

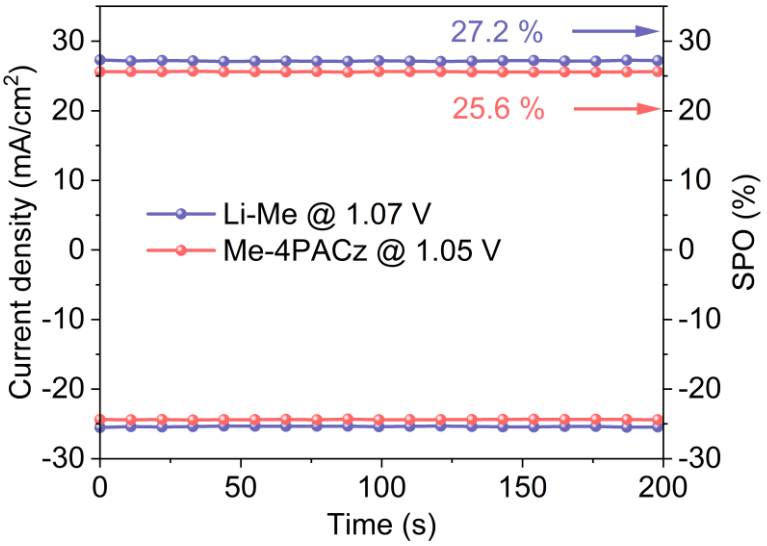

Supplementary Fig. 34 | Steady-state power output (SPO) of PSCs.

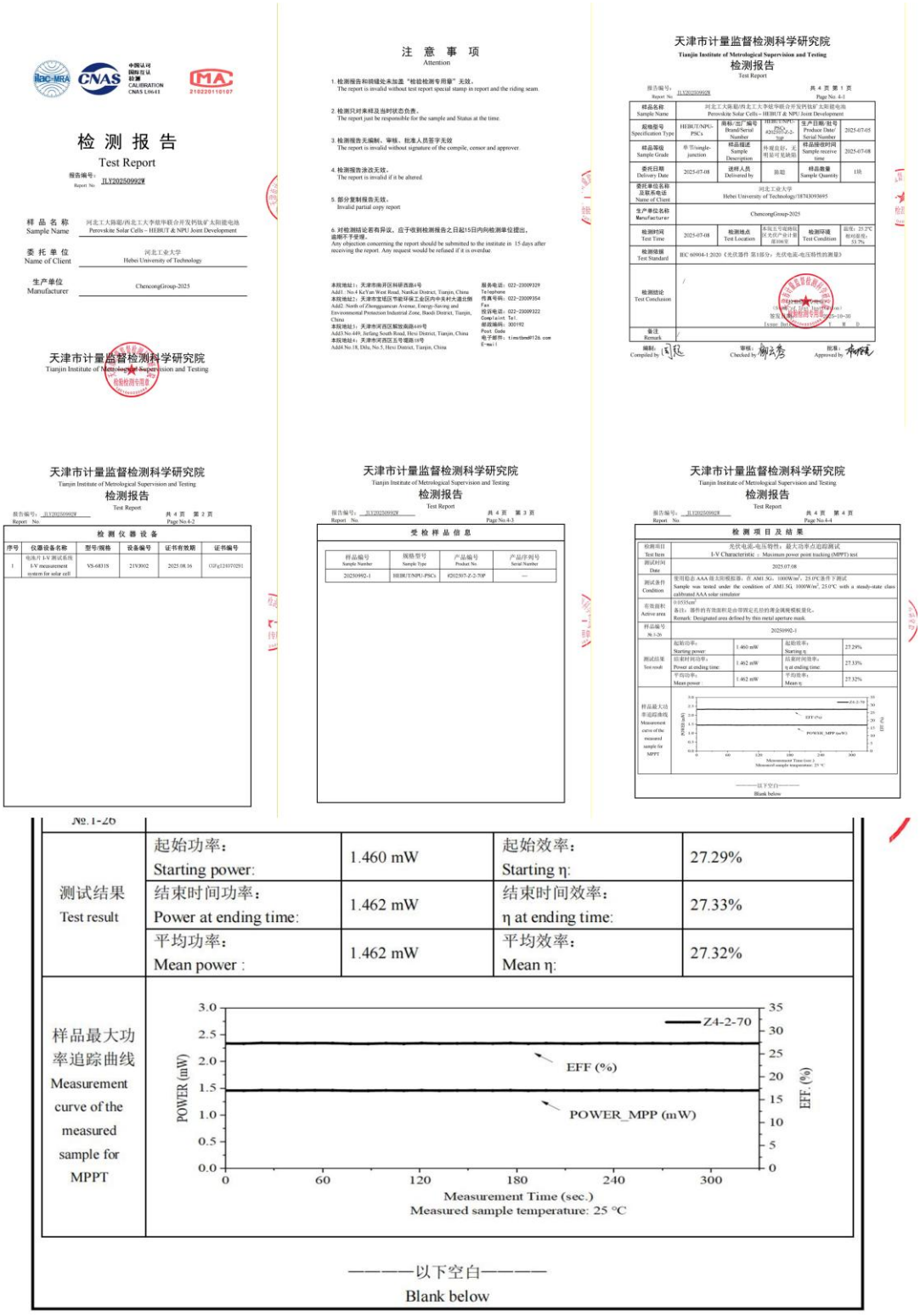

检 测 报 告

Test Report

报告编号 Report No. JLY20250992#

样品名称 Sample Name: 河北工大陈聪/西北工大李世华联合开发钙钛矿太阳能电池 Perovskite Solar Cells – HEBUT & NPU Joint Development

委托单位 Name of Client: 河北工业大学 Hebei University of Technology

生产单位 Manufacturer: ChencongGroup-2025

天津市计量监督检测科学研究院

Tianjin Institute of Metrological Supervision and Testing

注 意 事 项

Attention

1. 检测报告和骑缝处未加盖“检验检测专用章”无效。
The report is invalid without test report special stamp in report and the riding seam.

2. 检测只对来样及当时状态负责。
The report just be responsible for the sample and Status at the time.

3. 检测报告无编制、审核、批准人员签字无效
The report is invalid without signature of the compile, censor and approver.

4. 检测报告涂改无效。
The report is invalid if it be altered.

5. 部分复制报告无效。
Invalid partial copy report

6. 对检测结论若有异议，应于收到检测报告之日起15日内向检测单位提出，逾期不予受理。
Any objection concerning the report should be submitted to the institute in 15 days after receiving the report. Any request would be refused if it is overdue.

本院地址1：天津市南开区科研西路6号 Add1：No.4 KeYan West Road, Nankai District, Tianjin, China
本院地址2：天津市宝坻区节能环保工业区内中关村大道北侧 Add2: North of Zhongguancun Avenue, Energy-Saving and Environmental Protection Industrial Zone, Baodi District, Tianjin, China
本院地址3：天津市河西区解放南路449号 Add3:No.449, Jiefang South Road, Hexi District, Tianjin, China
本院地址4：天津市河西区五号堤路19号 Add4:No.19, Dihe, No.5, Hexi District, Tianjin, China

服务电话：022-23009329 Telephone
传真号码：022-23009354 Fax
投诉电话：022-23009322 Complaint Tel
邮政编码：300192 Post Code
电子邮件：timstlm@126.com E-mail

天津市计量监督检测科学研究院

Tianjin Institute of Metrological Supervision and Testing

检测报告

Test Report

共 4 页 第 1 页 Page No.4-1

样品名称 Sample Name	河北工大陈聪/西北工大李世华联合开发钙钛矿太阳能电池 Perovskite Solar Cells – HEBUT & NPU Joint Development			
起检型号 Specification Type	HEBUT/NPU-PSCs	商标/出厂编号 Brand/Serial Number	HEBUT/NPU-PSCs-Z-2-70#	生产日期/批号 Produce Date/ Serial Number: 2025-07-05
样品等级 Sample Grade	单节/single-junction	样品描述 Sample Description	外观良好，无明显可见缺陷	样品接收时间 Sample receive time: 2025-07-08
委托日期 Delivery Date	2025-07-08	送样人员 Delivered by	陈聪	样品数量 Sample Quantity: 1块
委托单位名称及联系电话 Name of Client	河北工业大学 Hebei University of Technology/18743093695			
生产单位名称 Manufacturer	ChencongGroup-2025			
检测时间 Test Time	2025-07-08	检测地点 Test Location	本院五号堤路校区光伏产业计量部406室	检测环境 Test Condition: 温度：25.2℃ 相对湿度：53.7%
检测依据 Test Standard	IEC 60904-1:2020《光伏器件 第1部分：光伏电流-电压特性的测量》			
检测结论 Test Conclusion	/			
备注 Remark	/			

编制 Compiled by: 审核 Checked by: 批准 Approved by:

天津市计量监督检测科学研究院

Tianjin Institute of Metrological Supervision and Testing

检测报告

Test Report

共 4 页 第 2 页 Page No.4-2

检 测 仪 器 设 备

序号	仪器设备名称	型号/规格	设备编号	证书有效期	证书编号
1	电池片 I-V 测试系统 I-V measurement system for solar cell	VS-6831S	21V3002	2025.08.16	023Y(c)20070251

天津市计量监督检测科学研究院

Tianjin Institute of Metrological Supervision and Testing

检测报告

Test Report

共 4 页 第 3 页 Page No.4-3

受 检 样 品 信 息

样品编号 Sample Number	规格型号 Sample Type	产品编号 Product No.	产品序列号 Serial Number
20250992-1	HEBUT/NPU-PSCs	#2025?-Z-2-70#	—

天津市计量监督检测科学研究院

Tianjin Institute of Metrological Supervision and Testing

检测报告

Test Report

共 4 页 第 4 页 Page No.4-4

检 测 项 目 及 结 果

检测项目 Test Item	光伏电流-电压特性，最大功率点追踪测试 I-V Characteristic ， Maximum power point tracking (MPPT) test			
测试时间 Date	2025.07.08			
测试条件 Condition	使用稳态 AAA 级太阳模拟器，在 AM1.5G，1000W/m²，25.0℃条件下测试 Sample was tested under the condition of AM1.5G, 1000W/m², 25.0℃ with a steady-state class calibrated AAA solar simulator			
有效面积 Active area	0.0553cm² 备注：器件的有效面积是由带阴定孔径的薄金属掩模板量化。 Remark: Designated area defined by thin metal aperture mask.			
样品编号 No.1-26	20250992-1			
测试结果 Test result	起始功率： Starting power:	1.460 mW	起始效率： Starting η:	27.29%
	结束时间功率： Power at ending time:	1.462 mW	结束时间效率： η at ending time:	27.33%
	平均功率： Mean power :	1.462 mW	平均效率： Mean η:	27.32%
样品最大功率追踪曲线 Measurement curve of the measured sample for MPPT				

以下空白 Blank below

№.1-26

测试结果 Test result	起始功率： Starting power:	1.460 mW	起始效率： Starting η:	27.29%
	结束时间功率： Power at ending time:	1.462 mW	结束时间效率： η at ending time:	27.33%
	平均功率： Mean power :	1.462 mW	平均效率： Mean η:	27.32%

样品最大功率追踪曲线 Measurement curve of the measured sample for MPPT

————以下空白————

Blank below

Supplementary Fig. 35 | Certification of the photovoltaic performance of a PSC. The best-performing target device certified by Tianjin Institute of Metrological Supervision and Testing, showing an average steady-state efficiency of 27.32%.

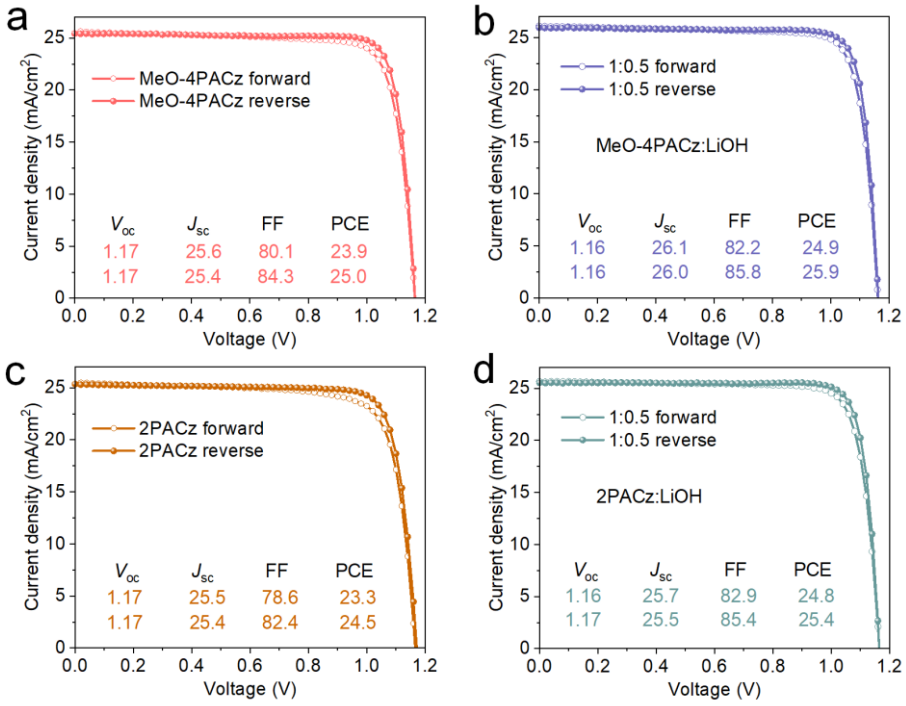

Supplementary Fig. 36 |Photovoltaic performance of PSCs prepared on different SAMs. (**a**) *J-V* curves of a device based on NiO_x-NPs/MeO-4PACz HTL. (**b**) *J-V* curves of a device based on a HTL of NiO_x-NPs/MeO-4PACz:LiOH=1:0.5. (**c**) *J-V* curves of a device based on a HTL of NiO_x-NPs/2PACz. (**d**) *J-V* curves of a device based on a HTL of NiO_x-NPs/2PACz:LiOH=1:0.5.

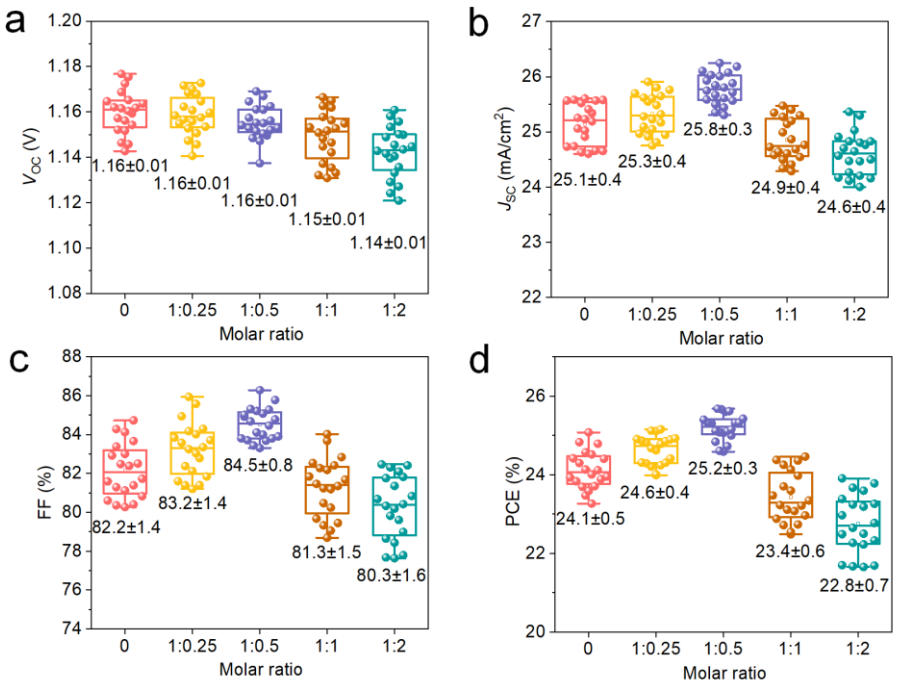

Supplementary Fig. 37 | Statistics of photovoltaic parameters of PSCs. (**a-d**) The distribution of photovoltaic parameters (V_{OC}, J_{SC}, FF, and PCE) obtained from 20 devices with various molar ratios of MeO-4PACz : LiOH.

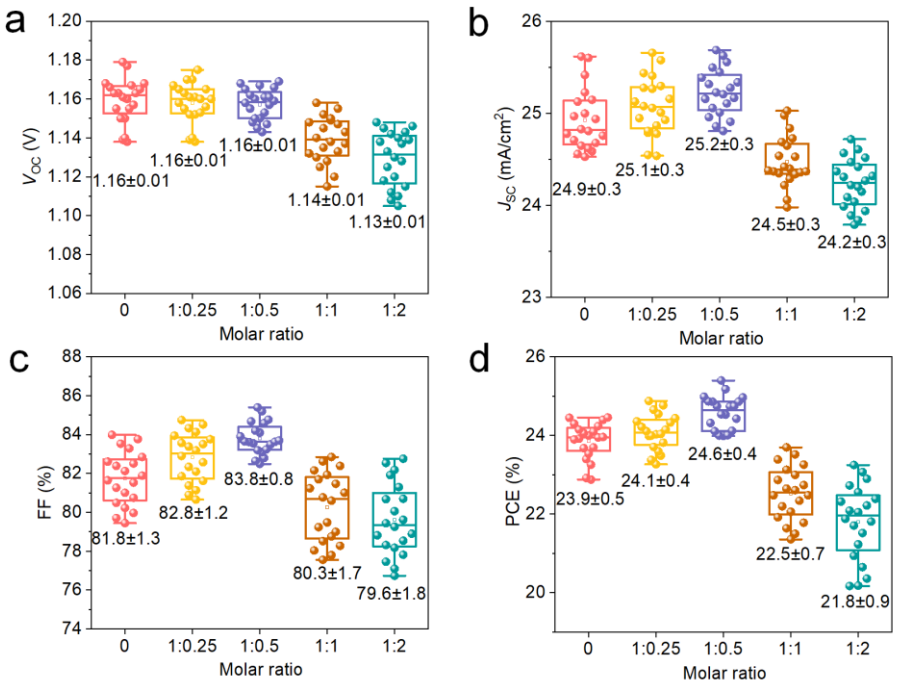

Supplementary Fig. 38 | Statistics of photovoltaic parameters of PSCs. (**a-d**) The distribution of photovoltaic parameters (V_{OC}, J_{SC}, FF, and PCE) obtained from 20 devices with various molar ratios of 2PACz : LiOH.

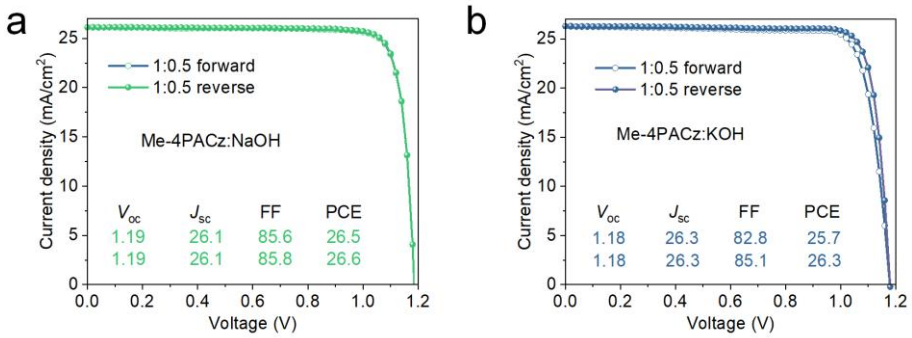

Supplementary Fig. 39 | Changes in the photovoltaic performance induced by other alkali treatments for Me-4PACz. (**a**) *J-V* curves of a device based on a HTL of NiO_x-NPs/Me-4PACz:NaOH=1:0.5. (**b**) *J-V* curves of a device based on a HTL of NiO_x-NPs/Me-4PACz:KOH=1:0.5.

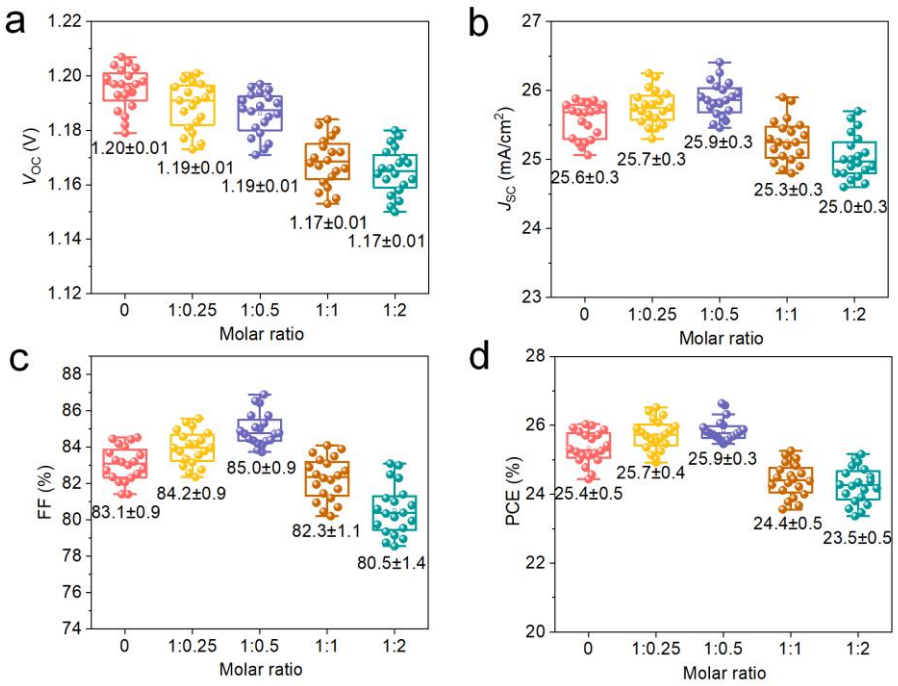

Supplementary Fig. 40 | Statistics of photovoltaic parameters of PSCs. (a-d) Photovoltaic parameters (V_{OC}, J_{SC}, FF, and PCE) obtained from 20 devices with various molar ratios of Me-4PACz : NaOH.

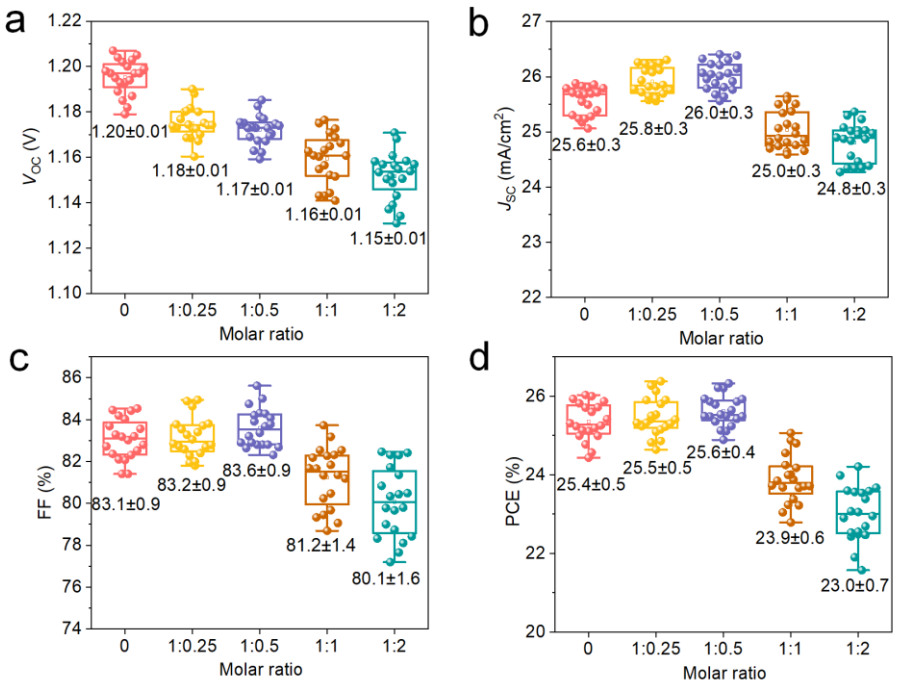

Supplementary Fig. 41 | Statistics of photovoltaic parameters of PSCs. (a-d) Photovoltaic parameters (V_{OC}, J_{SC}, FF, and PCE) obtained from 20 devices with various molar ratios of Me-4PACz : KOH.

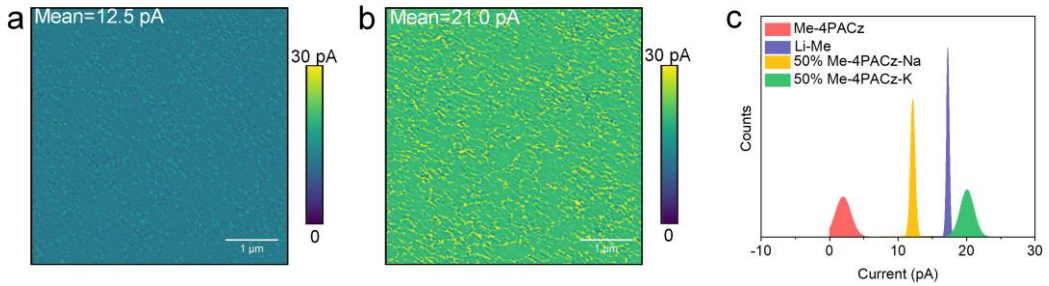

Supplementary Fig. 42 | C-AFM images of SAM layers on NiO_x-NPs/ITO surfaces. C-AFM imaging of (**a**) 50% Me-4PACz-Na and (**b**) 50% Me-4PACz-K under a bias voltage of +500 mV. (**c**) Current statistical distribution in C-AFM.

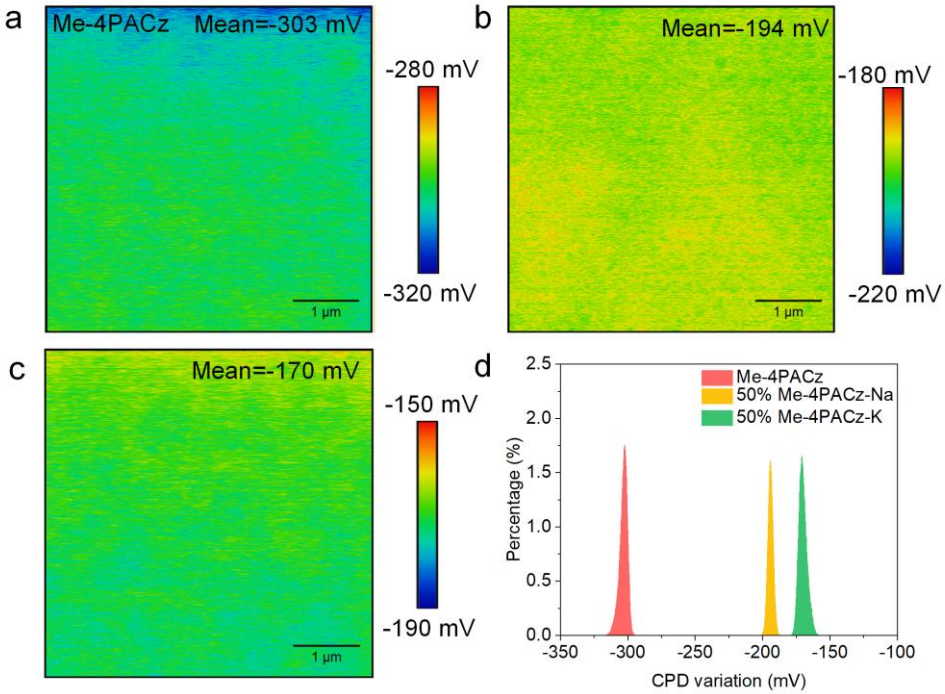

Supplementary Fig. 43 | KPFM characterization of SAM layers. KPFM images of (**a**) NiO_x-NPs/Me-4PACz, (**b**) NiO_x-NPs/50% Me-4PACz-Na, and (**c**) NiO_x-NPs/50% Me-4PACz-K. (**d**) Potential statistical distribution in KPEM.

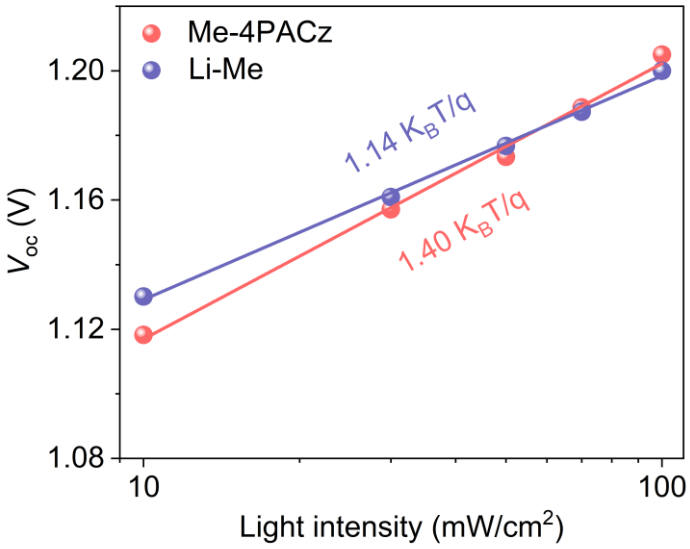

Supplementary Fig. 44 | Variation of V_{OC} in PSCs with changing light intensity.

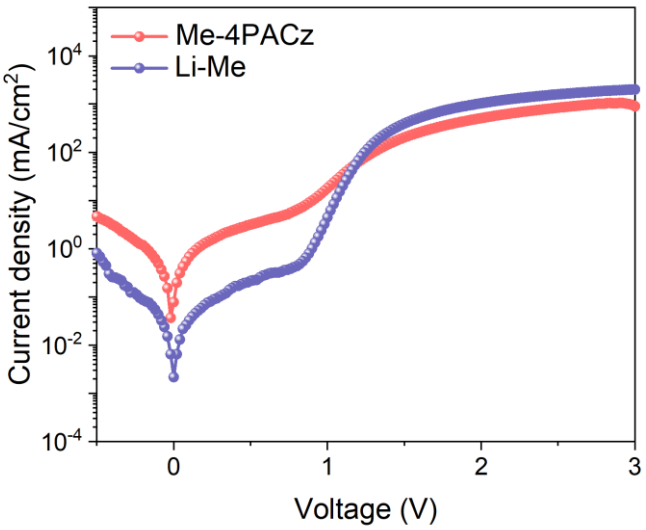

Supplementary Fig. 45 | Dark *J-V* curves of PSCs based on different SAM layers.

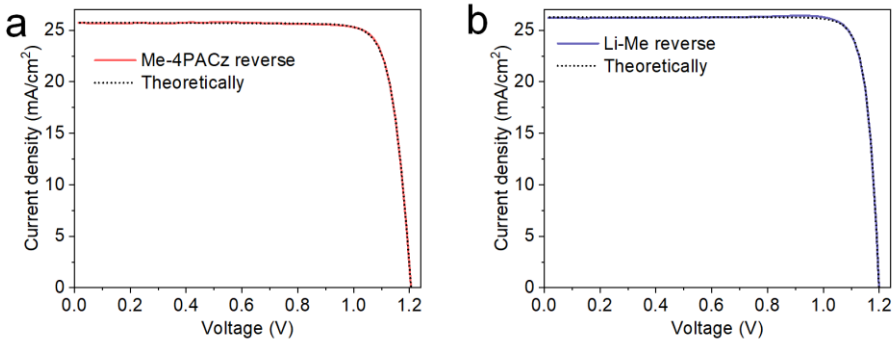

Supplementary Fig. 46 | The comparison of *J-V* curves between theoretical simulation and experimental measurement. Theoretically fitted *J-V* curves by modified detailed balance model and experimentally measured *J-V* characteristics for the PSCs based on (**a**) Me-4PACz/NiO_x-NPs and (**b**) Li-Me/NiO_x-NPs.

In order to understand the loss mechanism and qualify loss proportions (loss factors) of FF, the revised detailed balance model is used

$$J = \frac{V - JR_s}{R_{sh}} + J_n(V - JR_s) + J_r(V - JR_s) - J_p$$

where V is the applied voltage, J_p is the photocurrent, J_r and J_n are the current loss due to the radiative bimolecular emission and the nonradiative defect-induced recombination, respectively. R_s is the series resistance, which describes the ohmic loss by the contacts, carrier transport layers, and the hetero-junction interfaces between the perovskite and carrier transport layers. The defects, pinholes and voids induced current leakage is represented by the shunt resistance R_{sh}.

The photocurrent is given by

$$J_p = q\int_0^\infty \alpha(\lambda, L)\frac{\Gamma(\lambda)\lambda}{hc_0}d\lambda$$

where c_0 is the speed of light in air, Γ is the AM 1.5 G spectrum of Sun, λ is the wavelength and q is the elementary charge. The absorptivity α is the ratio of power absorbed by the perovskite active layer over the power of incident Sunlight. It can be obtained by numerically solving Maxwell equation. The refractive indices of materials can be obtained by ellipsometer measurement.

The radiative current is written as

$$J_r(V - JR_s) = J_0^r\left[exp\left(\frac{q(V - JR_s)}{k_BT}\right) - 1\right]$$

where k_B is the Boltzmann constant and T is the Kelvin temperature. Here, the radiative saturation current J_0^r is of the form

$$J_0^r = q\int_0^\infty \alpha(\lambda, L)\frac{\Gamma_0(\lambda)\lambda}{hc_0}d\lambda$$

It is proportional to the spectral overlap integral between the absorptivity α and black-body (thermal) emission spectrum Γ_0 at room temperature (T=300 K).

For perovskite solar cells, the dominant nonradiative recombination is the defect-induced recombination. Thus, the nonradiative current reads

$$J_n(V - JR_s) = J_0^n\, exp\left(\frac{q(V - JR_s)}{2k_BT}\right),\quad J_0^n = qn_i\gamma_bL + qn_i\gamma_s = qn_i\gamma$$

where γ_b and γ_s are the bulk nonradiative recombination rate and surface one, respectively, L is the perovskite active layer thickness, and n_i is the intrinsic carrier density of the perovskite material.

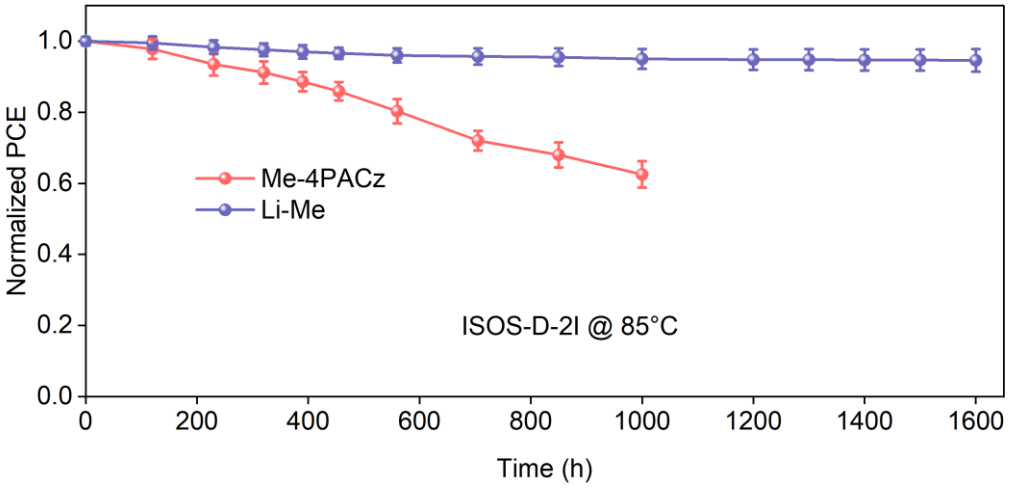

Supplementary Fig. 47 | Thermal stability of the PSCs based on Me-4PACz/NiO_x-NPs and Li-Me/NiO_x-NPs at 85 °C (the average PCE is obtained from 10 devices of each type of device, and the error bars represent the standard deviation of the devices)**.**

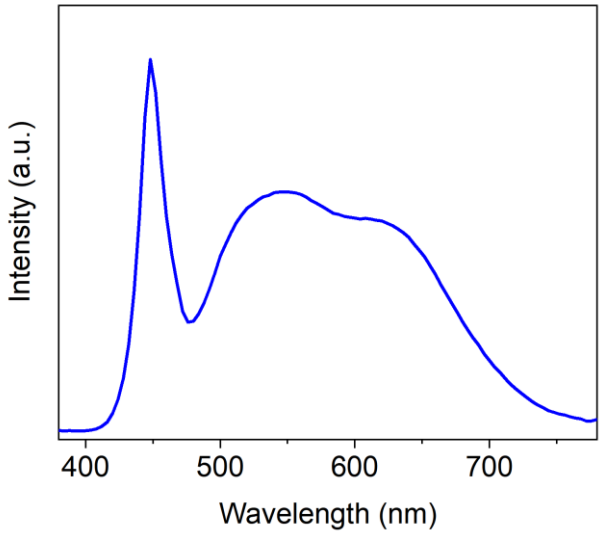

Supplementary Fig. 48 | The light spectra of the LED lamp used for MPP tracking stability tests.

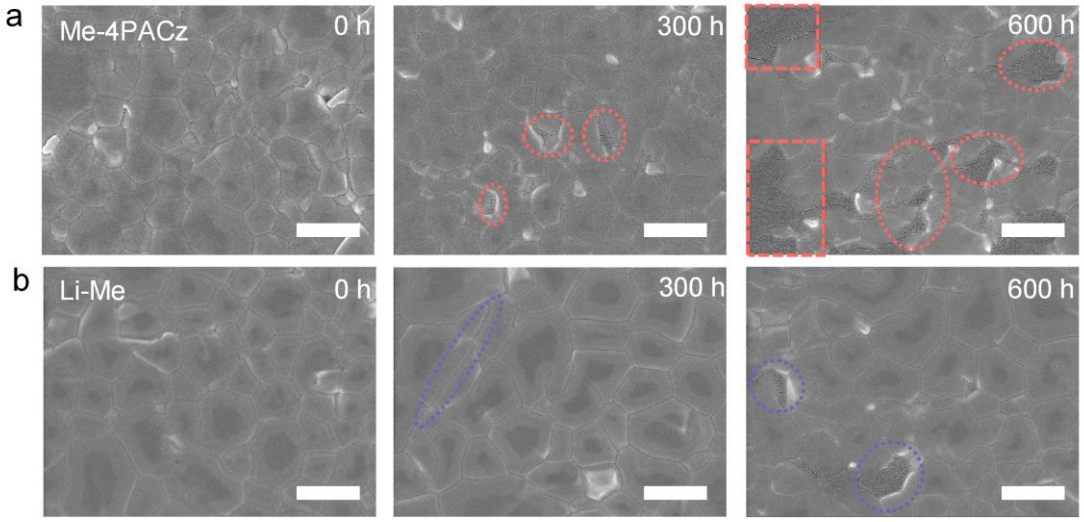

Supplementary Fig. 49 | Changes of perovskite bottom surface morphology with heating time. Morphology of the perovskite bottom on (**a**) Me-4PACz/NiO_x-NPs and (**b**) Li-Me/NiO_x-NPs before and after aging at 85 °C for different periods of time (the scale is 1 μm and the dashed area represents the amorphous region).

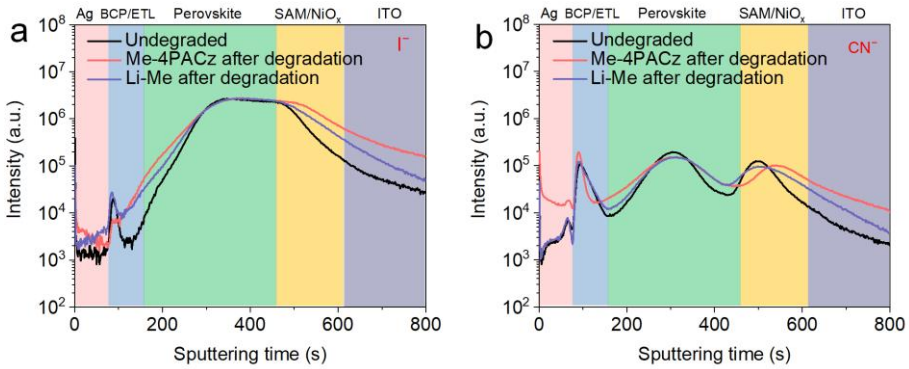

Supplementary Fig. 50 | Ion migration of perovskite films after degradation. (**a-b**) TOF-SIMS depth profiles of PSC devices based Me-4PACz and Li-Me before and after thermal aging at 85°C for 300 hours in N_2 atmosphere. I^- and CN^- (FA^+, MA^+) are selected for following the evolution of the perovskite film.

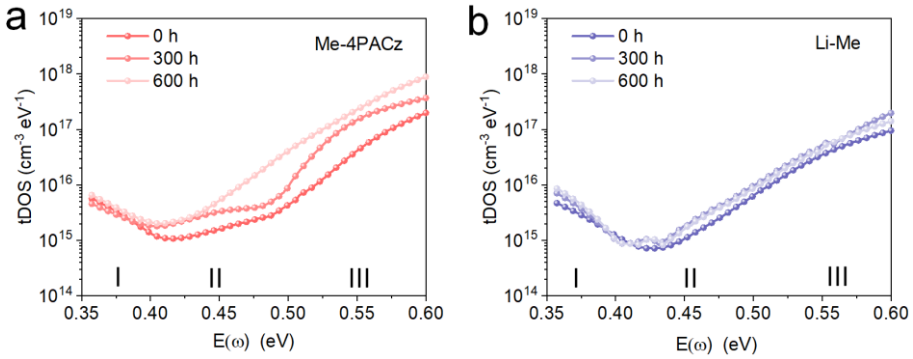

Supplementary Fig. 51 | Defect density versus aging time. Trap density of (**a**) NiO_x-NPs/Me-4PACz and (**b**) NiO_x-NPs/Li-Me -based PSCs heated at 85 °C for different periods.

Supplementary Table 1. The fitting parameters for the TRPL curves of perovskite films coated on Me-4PACz and Li-Me.

Sample	τ_1 [μs]	A_1	τ_2 [μs]	A_2	τ_{ave} [μs]
Me-4PACz	0.31	0.28	1.65	0.41	1.50
Li-Me	0.24	0.36	2.78	0.31	2.55

$$\tau_{ave} = \frac{A_1\tau_1^2 + A_2\tau_2^2}{A_1\tau_1 + A_2\tau_2}$$

Supplementary Table 2. Surface densities of SAM molecules and resultant PCEs of PSCs.

Materials/Methods	Control (molecules/cm^2)	After modification (molecules/cm^2)	Surface density variation	PCE	Certified PCE	Year/Ref.
4PATTI-C3/ 4PATTI-C4	9.00×10^{12}	9.63×10^{12}	7.00%	21.7%	N.A.	2024[18]
3PATAT-C3/ MeO-2PACz	1.60×10^{13}	1.00×10^{13}	-37.5%	23.0%	N.A.	2023[19]
CbzNaph solution	2.48×10^{13}	3.84×10^{13}	54.84%	24.98%	N.A.	2023[20]
2PACz+3-MPA	2.3×10^{13}	3.9×10^{13}	69.57%	25.3%	24.8%	2023[7]
Py3/2PACz	3.39×10^{15}	3.31×10^{15}	-2.36%	26.1%	25.7%	2024[21]
Li-Me/Me-4PACz	7.25×10^{13}	8.50×10^{13}	17.24%	27.3%	27.3%	**This Work**

Supplementary Table 3. Comparison of the operational stability of PSCs.

Device structure	Champion PCE (certified PCE)	Light source	Ageing condition	PCE_t/PCE_0 *	Reference
ITO/perovskite+DMAcPA/PCBM/BCP/Ag	25.9% (25.4%)	White LED	Air, 50% RH, 25 °C, 1000 h	96.6%	Nature, 2023[22]
ITO/NiO_x/MeO-4PADBC/perovskite/C60/BCP/Ag	25.6% (25.6%)	White LED	N_2, 65 °C, 1200 h	90%	Science, 2023[23]
FTO/Ph-4PACz/perovskite/C60/BCP/Ag	25.2% (24.4%)	White LED	N_2, 85% RH, 600 h	100%	Nat. Photonics，2024[24]
ITO/Me-4PACz/perovskite/C60/BCP/Ag	24.5% (N.A.)	White LED	N_2, 40-45 °C, 1200 h	91%	Nat. Energy, 2023[25]
ITO/2PACz/perovskite/C60/BCP/Cu	25.1% (24.7%)	White LED	Air, 60±10% RH, 25±5 °C, 1000 h	90%	Nat. Commun., 2024[8]
ITO/DC-TMPS/perovskite/PEAI/C60/ZnO/Au	24.8% (24.6%)	Xenon lamp	85 °C, 1200 h	98.2%	Science, 2024[26]
ITO/Py3/perovskite/OAmI/LiF/C60/BCP/Ag	26.1% (25.7%)	White LED	55 °C, 600 h	99%	Nature, 2024[21]
ITO/NiO_x/Me-Ph*p*PACz/perovskite/C60/BCP/Cu	26.2% (26.1%)	White LED	N_2, 50±10 °C, 3000 h	95.09%	Joule, 2024[27]
ITO/NiO_x/Me-4PACz/perovskite/PCBM/SnO_2/ITO/Cu	25.5% (25.2%)	White LED	50 °C,1000 h	85.4%	Science, 2023[28]
ITO/2PACz+Me-4PACz/perovskite/C60/SnO_2/Ag	26.9 (26.2%)	White LED	Air, 50% RH, 65 °C, 1200 h	95%	Science, 2024[29]
ITO/GM-4PACz/perovskite/PCBM/BCP/Ag	25.5% (N.A.)	White LED	Air, 30±5% RH, 25 °C, 1000 h	91.75%	Angew. Chem. Int. Ed., 2024[30]
ITO/NiO_x/perovskite/C60/BCP/Ag	26.7 (26.1%)	White LED	1000 h	80%	Adv Mater., 2024[31]
ITO/Me-4PACz+MeO-2PACz/perovskite/CPMAC/ALD-SnO_x/Ag	26.1% (N.A.)	N.A.	N_2, 65 °C, 2100 h	97.6%	Science, 2025[32]
ITO/PTAA/perovskite/CPMAC/ALD-SnO_x/Ag			N_2, 85 °C, 1500 h	95.0%	
ITO/2PACz/perovskite/PMMA/graphene/PC61BM/BCP/Au	24.6% (N.A.)	White LED	N_2, 90 °C, 3670 h	97.3%	Science, 2025[33]
ITO/PTAA/MoS_2/perovskite/MoS_2/C60/BCP/Ag	26.2% (25.9%)	N.A.	Air, 85 °C, 1200 h	>96%	Science, 2025[34]
ITO/PTAA/perovskite/C60/SnO_2/ITO/Au	23.1% (N.A.)	Metal-Halide Lamps	N_2, 85 °C, 622 h	99%	Science, 2025[35]
ITO/MPA-CPA/perovskite/Nd@C_{82}/C60/BCP/Ag	26.8% (26.3%)	White LED	Air, 50% RH, 65 °C, 2500 h	82%	Nature, 2025[36]
ITO/NiO_x/Li-Me/perovskite/C60/BCP/Cr/Au	27.3% (27.3%)	White LED	Air, 50% RH, 65 °C, 2000 h	94.5%	**This work**
			Air, 50% RH, 85 °C, 1000 h	93.3%	

[*] PCE_0 and PCE_t are the efficiencies of devices before and after stability tests.

References

1 Wang, S. J. *et al.* Critical role of removing impurities in nickel oxide on high-efficiency and long-term stability of inverted perovskite solar cells. *Angew. Chem. Int. Ed.* **61**, e202116534, (2022).

2 Neese, F. *et al.* The ORCA quantum chemistry program package. *J. Chem. Phys.* **152**, 224108, (2020).

3 Kresse, G. *et al.* Efficient iterative schemes for ab initio total-energy calculations using a plane-wave basis set. *Phys. Rev. B* **54**, 11169–11186, (1996).

4 Liu, S. *et al.* Buried interface molecular hybrid for inverted perovskite solar cells. *Nature* **632**, 536–542, (2024).

5 Grimme, S. *et al.* Dispersion-corrected mean-field electronic structure methods. *Chem. Rev.* **116**, 5105–5154, (2016).

6 Thompson, A. P. *et al.* LAMMPS - a flexible simulation tool for particle-based materials modeling at the atomic, meso, and continuum scales. *Computer Phys. Commun.* **271**, 108171, (2022).

7 Park, S. M. *et al.* Low-loss contacts on textured substrates for inverted perovskite solar cells. *Nature* **624**, 289–294, (2023).

8 Li, D. *et al.* Co-adsorbed self-assembled monolayer enables high-performance perovskite and organic solar cells. *Nat.Commun.* **15**, 7605, (2024).

9 Martinez, L. *et al.* PACKMOL: a package for building initial configurations for molecular dynamics simulations. *J. Chem. Phys.* **30**, 2157-2164, (2009).

10 Jorgensen, W. L. *et al.* Development and testing of the OPLS all-atom force field on conformational energetics and properties of organic liquids. *J. Am. Chem. Soc.* **118**, 11225–11236, (1996).

11 Kanhaiya, K. *et al.* Accurate force fields for atomistic simulations of oxides, hydroxides, and organic hybrid materials up to the micrometer scale. *J. Chem. Theory Comput.* **19**, 8293–8322, (2023).

12 Stukowski, A. Visualization and analysis of atomistic simulation data with OVITO–the open visualization tool. *Modelling Simul. Mater. Sci. Eng.* **18**, 015012, (2010).

13 Zhou, Y. *et al.* Interfacial mdification of NiO_x for highly efficient and stable inverted provskite solar cells. *Adv. Energy Mater.* **14**, 2400616, (2024).

14 Rolston, N. *et al.* Engineering stress in perovskite solar cells to improve stability. *Adv. Energy Mater.* **8**, 1802139, (2018).

15 Hu, Q. X. *et al.* Optimization of perovskite/carbon interface performance using N-doped coal-based graphene quantum dots and its mechanism analysis. *J. Energy Chem.* **79**, 242-252, (2023).

16 Liu, D. C. *et al.* Polymerization strategies to construct a 3D polymer passivation network toward high performance perovskite solar cells. *Angew. Chem. Int. Ed.* **62**, e202301574, (2023).

17 Ye, S. Y. *et al.* A breakthrough efficiency of 19.9% obtained in inverted perovskite solar cells by using an efficient trap state passivator Cu(thiourea)I. *J. Am. Chem. Soc.* **139**, 7504-7512, (2017).

18 Truong, M. A. *et al.* Tetrapodal hole-collecting monolayer materials based on saddle-like cyclooctatetraene core for inverted perovskite solar cells. *Angew. Chem. Int. Ed.* **63**, e202412939, (2024).

19 Truong, M. A. *et al.* Tripodal triazatruxene derivative as a face-on oriented hole-collecting monolayer for efficient and stable inverted perovskite solar cells. *J. Am. Chem. Soc.* **145**, 7528–7539, (2023).

20 Liu, M. *et al.* Compact hole-selective self-assembled monolayers enabled by disassembling micelles in solution for efficient perovskite solar cells. *Adv. Mater.* **35**, e2304415, (2023).

21 Zhao, K. *et al.* peri-Fused polyaromatic molecular contacts for perovskite solar cells. *Nature* **632**, 301–306, (2024).

22 Tan, Q. *et al.* Inverted perovskite solar cells using dimethylacridine-based dopants. *Nature* **620**, 545–551, (2023).

23 Li, Z. *et al.* Stabilized hole-selective layer for high-performance inverted p-i-n perovskite solar cells. *Science* **382**, 284–289, (2023).

24 Wang, X. *et al.* Regulating phase homogeneity by self-assembled molecules for enhanced efficiency and stability of inverted perovskite solar cells. *Nat. Photonics* **18**, 1269–1275, (2024).

25 Zheng, X. *et al.* Co-deposition of hole-selective contact and absorber for improving the processability of perovskite solar cells. *Nat. Energy* **8**, 462–472 (2023).

26 Tang, H. *et al.* Reinforcing self-assembly of hole transport molecules for stable inverted perovskite solar cells. *Science* **383**, 1236–1240, (2024).

27 Qu, G. *et al.* Conjugated linker-boosted self-assembled monolayer molecule for inverted perovskite solar cells. *Joule* **8**, 2123–2134, (2024).

28 Yu, S. *et al.* Homogenized NiO_x nanoparticles for improved hole transport in inverted perovskite solar cells. *Science* **382**, 1399–1404, (2023).

29 Chen, H. *et al.* Improved charge extraction in inverted perovskite solar cells with dual-site-binding ligands. *Science* **384**, 189–193, (2024).

30 Zhou, H. *et al.* Glycol monomethyl ether-substituted carbazolyl hole-transporting material for stable inverted perovskite solar cells with efficiency of 25.52%. *Angew. Chem. Int. Ed.* **63**, e202403068, (2024).

31 Huang, Y. *et al.* High-efficiency inverted perovskite solar cells via in situ passivation directed crystallization. *Adv. Mater.* **36**, e2408101, (2024).

32 You, S. *et al.* C_{60}-based ionic salt electron shuttle for high-performance inverted perovskite solar modules. *Science* **6750**, 964–968, (2025).

33 Li, Q. *et al.* Graphene-polymer reinforcement of perovskite lattices for durable solar cells. *Science* **387**, 1069–1077, (2025).

34 Zai, H. *et al.* Wafer-scale monolayer MoS_2 film integration for stable, efficient perovskite solar cells. *Science* **387**, 186–192, (2025).

35 Zhang, Y. *et al.* Nonalloyed α-phase formamidinium lead triiodide solar cells through iodine intercalation. *Science* **387**, 284–290, (2025).

36 Lin, Y. *et al.* A Nd@C_{82}-polymer interface for efficient and stable perovskite solar cells. *Nature* **642**, 78–84, (2025).